1
Gold Nanoshells in Biomedical Applications

Tim A. Erickson and James W. Tunnell

1.1
Introduction

Gold nanoshells are spherical particles with diameters typically ranging in size from 10 to 200 nm (Figure 1.1). They are composed of a dielectric core covered by a thin gold shell. As novel nanostructures, they possess a remarkable set of optical, chemical and physical properties, which make them ideal candidates for enhancing cancer detection, cancer treatment, cellular imaging and medical biosensing.

Gold nanoshells are unique in that they combine many ideal features in a single particle. As a direct result of nanoscale resonance phenomena, gold nanoshells have very large optical absorption and scattering cross-sections, which render them highly suitable as contrast agents for imaging. They can be tuned to preferentially absorb or scatter light at specific wavelengths in the visible and near-infrared (NIR) regions of the spectrum. In the NIR 'tissue window', light penetration into tissue is optimal. Nanoshells tuned to absorb NIR radiation are particularly useful as mediators of photothermal cancer therapy because they efficiently convert absorbed radiation into heat, and are thermally stable at therapeutic temperatures. Furthermore, nanoshells preferentially accumulate at tumor sites due to their nanoscale dimensions. The inert gold surface of nanoshells provides several advantages, including biocompatibility, noncytotoxicity, and it also facilitates conjugation to monoclonal antibodies or other biomolecules for both active tumor targeting and biosensing applications.

The first Stage I clinical trials using nanoshells as therapeutic agents to treat head and neck cancers are set to commence in 2008 [2]. Over the past few years, the pace of research in this field has accelerated rapidly, as have the number of potential biomedical applications for nanoshells. It has been the present authors' best attempt to keep abreast of new developments in the field but, given the pace of progress, this chapter will be partially outdated by the time it hits the press – which is good news! The chapter is designed with two distinct audiences in mind: researchers already in the field who may use it as a quick reference; and 'early-stage' researchers, who can use it as a first read to gain a broader understanding

Nanomaterials for the Life Sciences Vol. 3: Mixed Metal Nanomaterials. Edited by Challa S. S. R. Kumar

ISBN: 978-3-527-32153-7

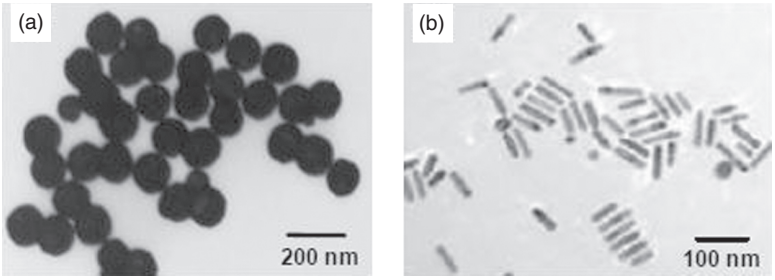

Figure 1.1 Transmission electron microscopy images of (a) gold nanoshells and their gold nanoparticle counterparts (b) gold nanorods. The size distribution typically has a standard deviation from the mean of 10–20% [1].

of the field. It is organized in the following manner. The first section highlights the unique optical and material properties of nanoshells and explores the physics underlying the associated phenomena. The second section we describe the synthesis of nanoshells. The third section describes the transport, biodistribution and benign toxicity profile of nanoshells *in vivo*, while the fourth section concludes with an extensive discussion on the various biomedical applications of nanoshells. Although the focus of the chapter is on gold nanoshells, their nanoparticle counterparts – gold nanorods, gold nanospheres and quantum dots – will also be discussed, in order to provide relevant comparisons and contrasts.

1.2 Physical Properties of Gold Nanoshells

1.2.1 Overview of General Optical Properties

Before delving into a comprehensive analysis of the physics behind nanoshells, it is worthwhile to highlight their novel optical properties. Nanoshells function as useful and versatile imaging agents because of their large extinction cross-sections, immunity to photobleaching, spectral tunability, absorption/scattering ratio tunability, electromagnetic near-field enhancement, and enhanced luminescence. These optical phenomena are in large part due to a resonance phenomenon, known as surface plasmon resonance, which is discussed in the next subsection.

The optical cross-sections and luminescent properties of gold nanoshells compare favorably with those of conventional fluorophores and quantum dots. Wu *et al*. found the absorption of a single 20 nm-diameter nanoshell to correspond to the absorption of 40 000 molecules of indocyanine green, a dye used as a photosensitizer in photodynamic therapy [3]. For nanoshells with a diameter of 130 nm, the optical extinction cross-section ($3.8 \times 10^{-14}\,m^2$) is more than one million times greater than the cross-section of an indocyanine green molecule ($1.66 \times 10^{-20}\,m^2$)

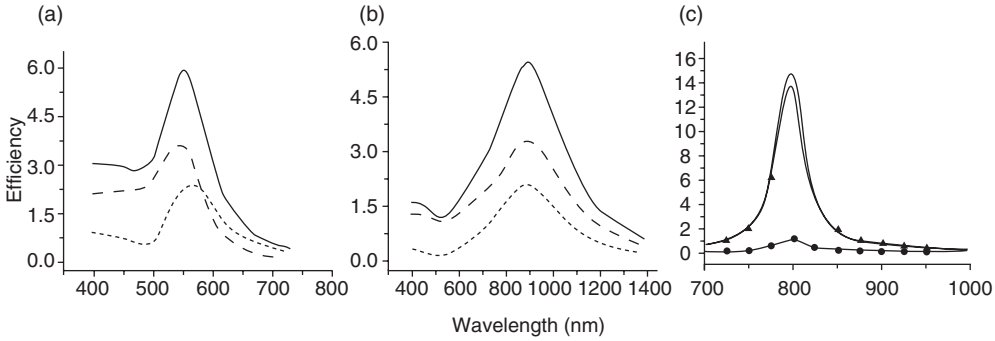

Figure 1.2 Calculated extinction (top curve), absorption (middle curve) and scattering (bottom curve) efficiencies for: (a) a 80 nm-diameter gold nanosphere; (b) a 70 nm-radius gold nanoshell with a 60 nm silica core; and (c) a 59.6 × 15.3 nm gold nanorod [6].

[4], and almost twice as great as the cross-section of a CdSe quantum dot ($1.5 \times 10^{14}\,m^2$) with the same radius [5]. The dimensionless extinction coefficient Q_{ext} of a gold nanoshells typically ranges from ~3 to 7, depending on nanoshell geometry, which is comparable to gold nanospheres, but less than half the *maximum* extinction coefficient of gold nanorods (~12–21) (Figure 1.2). In photoluminescence studies, Park *et al.* found both 120 nm gold nanoshells and 50 nm (long axis) gold nanorods to be 140 times brighter than 100 nm fluoresceinated polystyrene beads, which are commonly used in biological imaging applications [1]. This is similar to the results obtained by Wang *et al.*, who found the two-photon induced luminescence from a single gold nanorod to be almost 60-fold brighter than a single rhodamine 6G molecule [7].

An additional advantage of nanoshells and other gold nanoparticles is their photostability. In photoluminescence studies, they have not been found to photobleach [8]; conventional fluorophores are highly susceptible to photobleaching [9, 10]. Quantum dots, while being generally more resistant to photobleaching [11], suffer from intrinsic, intermittent emission or 'blinking' [12], which complicates sensitive imaging techniques.

Perhaps the most novel characteristic of gold nanoshells is their tunability. The position of the extinction (plasmon resonance) peak and the relative contributions of absorption and scattering to total extinction can be selected by configuring two parameters: the radii of the inner core (r_1); and the outer shell (r_2) (see Figure 1.7). For a given r_2, the position of the extinction peak is determined by the core to shell ratio (r_1/r_2) [13]. For greater core to shell ratios (thinner gold shells), the peak becomes shifted to longer wavelengths. For gold nanoshells, the position of the resonant extinction peak can be selectively tuned from 600 nm to greater than 1000 nm (Figure 1.3). This wavelength range is especially significant because it includes the 'NIR tissue window' from 700 to 900 nm, where tissue is most transparent to light. In the NIR region, effective (1/e) penetration depths vary from a

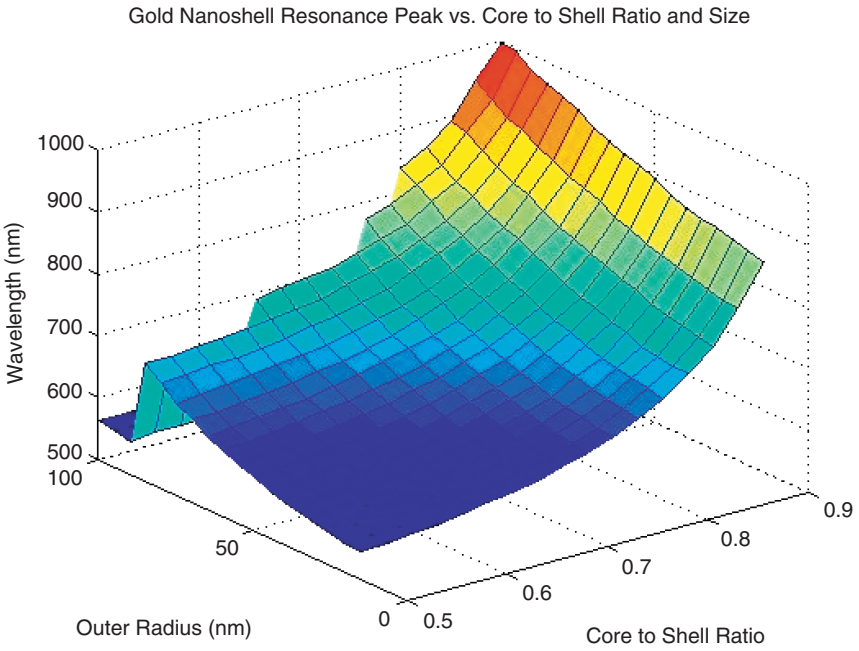

Figure 1.3 Gold nanoshell resonance peak versus core to shell ratio and size. Mie theory calculations of the plasmon resonance peak position as a function of nanoshell geometry from 500 to 1000 nm. Two trends are apparent. For a given nanoparticle size, the resonance peak can be selected by changing the core-to-shell ratio. Larger particles correspond to longer resonance peak wavelengths. The sharp drop-off for large nanoshells with smaller core-to-shell ratios is explained in Section 1.1.2.3.

few millimeters to several centimeters, depending on tissue type [14, 15]. The ability of nanoshells to be tuned to the NIR is central to their functionality for *in vivo* applications. Gold nanorods also exhibit spectral tunability across a broad range of wavelengths, including the NIR [6]; however, gold nanospheres may have limited use for certain applications because their resonance peak lies outside the NIR window at ~520 nm and their spectral tunability is very limited.

In addition to spectral tunability, the absorption to scattering ratio of nanoshells can also be tuned by changing the nanoshell's outer radius (r_2). For smaller nanoshells, absorption dominates scattering, whereas for larger nanoshells scattering dominates absorption. In between the two extremes, the contributions of absorption and scattering to total extinction can be made approximately equal (Figure 1.4). It is therefore possible to design nanoshells for dual imaging and photothermal therapy applications, where high scattering efficiencies facilitate scatter-based imaging and high absorption efficiencies facilitate photothermal therapy. By appropriately choosing the dimensions of r_1 and r_2, the position of the extinction peak and the relative amounts of absorption and scattering can be selected across a wide range of wavelengths, as demonstrated in Figures 1.3 and 1.4. This is a truly remarkable optical property, given that untold numbers of

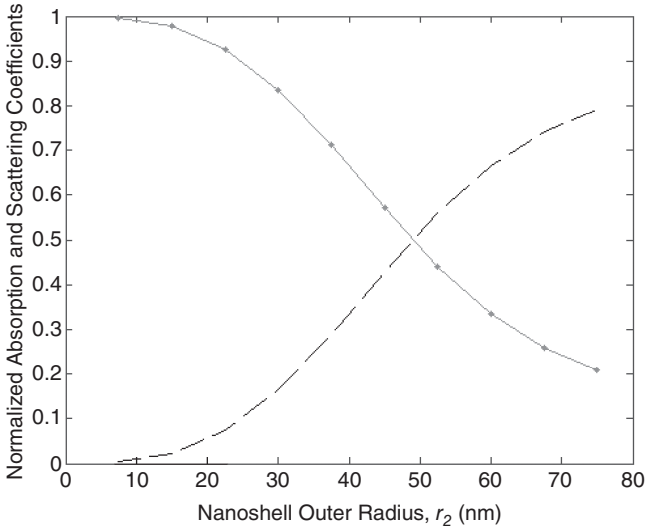

Figure 1.4 Absorption (solid line) and scattering (dashed line) coefficients calculated using Mie theory for a nanoshell with a fixed core-to-shell ratio of 0.8. For a nanoshell with an outer radius of 50 nm, the absorption and scattering efficiencies are almost equal. The normalized efficiencies were calculated by integrating the efficiencies between 500–1000 nm, and are thus indicative of the response to a broadband source.

conventional organic dyes would be required to cover the same spectral domain as geometrically tuned gold nanoshells.

Gold nanoshells and nanospheres exhibit another unique property, which is distinct from anything seen in conventional fluorophores. Metallic nanoparticles act as nanolenses, which efficiently focus incident electromagnetic radiation into the near-field region close to their surfaces with subwavelength precision [16, 17]. Jackson *et al.* have predicted near-field enhancements ($E_{enhancement} = E_{local}/E_{incident}$) of ~25 for silver nanoshells [18], while Averitt *et al.* have predicted local field enhancements of ~3 for gold nanoshells with outer radii of 12–15 nm [13]. Chien *et al.* have calculated enhancements of ~450 for assemblies of gold nanospheres (Figure 1.5), which can be thought of rows of nanolenses. Since the intensity scales as the electric field squared, these near-field enhancements produce intensity enhancements of many orders of magnitude. For the nanosphere assembly, the localized surface intensity would increase by a factor of over 200 000. Such enhancements have important applications in single molecule detection (see Section 1.5) [18].

1.2.2
The Physics of Gold Nanoshells

Nanoshells exhibit unique optical properties because their interaction with the electromagnetic field is greatly intensified by a phenomenon known as localized

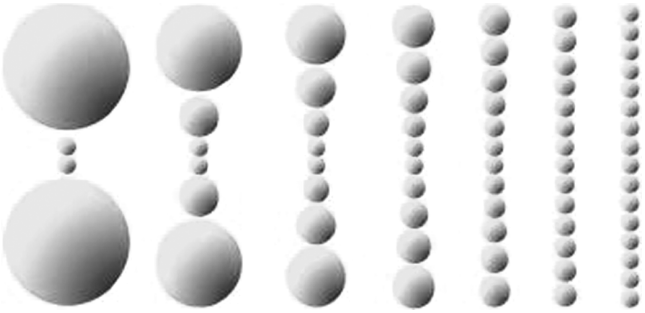

Figure 1.5 Gold nanosphere assemblies used in theoretical calculations by Chien *et al.* The length of each chain is fixed to equal 167.5 nm [16].

surface plasmon resonance (LSPR). This resonance effect arises from the collective oscillation of the conduction electrons in the gold shell, which efficiently couple to the incident electromagnetic field, and propagate along the surface [13, 19]. The quanta of these surface charge density oscillations is referred to as a surface plasmon polariton.

The LSPR of gold nanoshells at visible and NIR wavelengths is a physical possibility because of two key factors: (i) the dielectric function of gold at optical wavelengths; and (ii) their nanoscale dimensions. Several distinct phenomena must be 'connected' in order to provide a theoretical framework for understanding the interaction between gold nanoshells and optical electromagnetic fields. First, the dielectric function of gold at optical wavelengths will be introduced, after which the dielectric function of gold will be related to the resonant interaction of gold nanoshells with optical electromagnetic fields. The absorption and scattering properties of nanoshells will then be elucidated by using the quasi-static approximation. Lastly, Mie theory [20] and plasmon hybridization [21] will be introduced as rigorous analytical methods for calculating and understanding their optical phenomena.

1.2.2.1 **The Dielectric Function of Gold**

The most recent experimental data for the dielectric function of gold comes from measurements published by Johnson and Christy in 1972 [22]. Unfortunately, there are significant gaps in the data at visible/NIR wavelengths. However, theoretical models have been formulated to fit the data and provide good estimates across the visible and NIR spectra (Figure 1.6). The optimized Drude–Lorentz model of gold's dispersion described by Vial *et al.* provides an analytical fit to the data at optical frequencies [23]. It modifies the standard Drude dielectric approximation, by adding a single frequency-dependent Drude–Lorentz oscillator term (L), in order to account for interband transitions of bound electrons, which are excited by wavelengths shorter than ~550 nm. Mathematically, the Drude–Lorentz dielectric function is given by

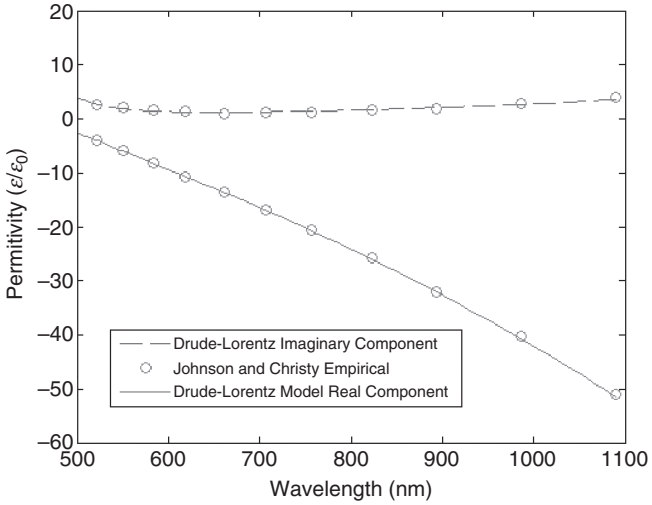

Figure 1.6 Complex dielectric function of gold consisting of both real and imaginary components. There is good agreement between the Johnson and Christy data points and the Drude–Lorentz model.

$$\varepsilon_{Drude-Lorentz}(\omega) = 1 - \frac{\omega_p^2}{\omega^2 + i\Gamma\omega} + L(\omega)$$

where ω_p is the volume plasma frequency of bulk gold, ω is the angular frequency of the electromagnetic field, and Γ is the damping coefficient or bulk collision frequency. The performance of the model in predicting the complex dielectric function of gold is depicted in Figure 1.6. The complex dielectric function of gold has a large, negative real component accounting for the reflectivity of bulk gold, and a smaller, positive imaginary component, which is associated with absorption. In the following section, we will show how gold's dielectric function is related to LSPR in gold nanoshells.

1.2.2.2 The Quasi-Static Approximation and Conditions for Surface Plasmon Resonance

In the following analysis, the nanoshell is modeled as shown in Figure 1.7, with inner radius r_1, outer radius r_2 and dielectric constants ε_1 (silica core = 2.13), ε_3 (surrounding aqueous medium = 1.78), and *dielectric function*, $\varepsilon_2(\omega)$, for the gold shell.

The quasi-static (dipole) approximation is a first-order approach, which describes the interaction between a gold nanoshell and electromagnetic radiation at optical frequencies [13]. In the quasi-static approximation, the incident electric field, $\boldsymbol{E(r,t)}$, is assumed not to vary spatially over the dimensions of the nanoshell, while maintaining its time-dependence so that $\boldsymbol{E(r,t)} = \boldsymbol{E}_o e^{-i\omega t}$. The quasi-static

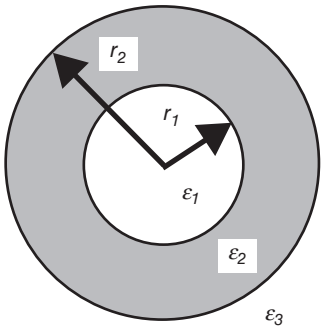

Figure 1.7 Schematic of gold nanoshell with indicated radii and three dielectric functions corresponding to the core, shell and ambient medium.

approximation is valid in the limit where the wavelength of incident light λ is much greater than the diameter d of the nanoshell ($\lambda >> d$). This is particularly accurate for nanoshells with radii of less than 40 nm [13]. Despite lacking rigor, the quasi-static approximation has several inherent advantages. As will be shown, it dramatically simplifies the mathematical analysis describing the nanoshell's interaction with the electric field and, more importantly, it provides a valuable physical interpretation of LSPR in gold nanoshells.

The solution for the electric field in the regions corresponding to the core (ε_1), shell (ε_2) and ambient medium (ε_3) is determined by solving Laplace's equation for the potential V in each region, then taking the gradient to determine the electric field $\boldsymbol{E}_i$ in each of the three regions, and finally adding the time-dependence ($e^{-i\omega t}$) [13]. The general solution for the potential in each region ($i = 1, 2, 3$) is

$$V_i = \left[A_i r + \left(B_i / r^2\right)\right]\cos(\theta)$$

with radius r, polar angle θ and coefficients A_i and B_i, which are determined by satisfying boundary conditions for continuity of the tangential component of the electric field and continuity of the normal component of the displacement field. After solving for V_i, the electric fields ($E_i = -\nabla V_i$) are calculated to be:

$$\boldsymbol{E}_1 = \frac{9\varepsilon_2\varepsilon_3}{\varepsilon_2\varepsilon_a + 2\varepsilon_3\varepsilon_b} E_o\left(\cos\theta\hat{r} - \sin\theta\hat{\theta}\right)$$

$$\boldsymbol{E}_2 = \frac{3\varepsilon_3}{\varepsilon_2\varepsilon_a + 2\varepsilon_3\varepsilon_b}\left[(\varepsilon_1 + 2\varepsilon_2) + 2(\varepsilon_1 - \varepsilon_2)\times(r_1/r)^3\right]E_o\cos\theta\hat{r} - \left[(\varepsilon_1 + 2\varepsilon_2) - (\varepsilon_1 - \varepsilon_2)(r_1/r)^3\right]E_o\sin\theta\hat{\theta}$$

$$\boldsymbol{E}_3 = \left(2\frac{\varepsilon_2\varepsilon_a - \varepsilon_3\varepsilon_b}{\varepsilon_2\varepsilon_a + 2\varepsilon_3\varepsilon_b}\frac{r_2^3}{r^3} + 1\right)E_o\cos(\theta)\hat{r} + \left(2\frac{\varepsilon_2\varepsilon_a - \varepsilon_3\varepsilon_b}{\varepsilon_2\varepsilon_a + 2\varepsilon_3\varepsilon_b}\frac{r_2^3}{r^3} - 1\right)E_o\sin(\theta)\hat{\theta}$$

where

$$\varepsilon_a = \varepsilon_1(3-2P) + 2\varepsilon_2 P$$

$$\varepsilon_b = \varepsilon_1 P + \varepsilon_2(3-P)$$

$$P = 1-(r_1/r_2)^3.$$

The induced field in the region outside the shell is the same as that of a *dipole* ($\boldsymbol{p} = \varepsilon_3\ \alpha\ \boldsymbol{E}_{\text{induced}}$) located at the center of the shell with polarizability,

$$\alpha(\omega) = 4\pi\varepsilon_o r_2^3 \left| \frac{\varepsilon_2\varepsilon_a - \varepsilon_3\varepsilon_b}{\varepsilon_2\varepsilon_a + 2\varepsilon_3\varepsilon_b} \right|, \text{ where } \varepsilon_o = 8.85\times 10^{-12}\,\text{Fm}^{-1}.$$

When the temporal oscillation of the electric field is taken into account, we arrive at a classical physical interpretation of surface plasmon resonance in a nanoshell. In the quasi-static limit, the dominant behavior of a gold nanoshell in an electric field at optical frequencies is that of an oscillating dipole. In this classical picture, resonance occurs when the polarizability α is maximized, or when the denominator in the above equation goes to zero. The condition for resonance is thus:

$$\varepsilon_2\varepsilon_a + 2\varepsilon_3\varepsilon_b = 0$$

In this simplified analysis, the polarizability goes to infinity when the resonance condition is satisfied because damping effects due to reaction radiation have been neglected [19]. When effects from reaction radiation are incorporated the effective polarizability becomes

$$\alpha_{\textit{effective}}(\omega) = \frac{\alpha(\omega)}{1 - i\dfrac{k^3}{6\pi\varepsilon_o}\alpha(\omega)}$$

It is instructive to observe how the resonance condition can be met for a generic nanoshell with a silica core and unknown shell dielectric function (ε_2). Figure 1.8 is a plot of $\varepsilon_2\varepsilon_a + 2\varepsilon_3\varepsilon_b$ versus the shell dielectric function (ε_2) for a $r_1 = 60\,\text{nm}$, $r_2 = 75\,\text{nm}$ nanoshell. As shown in Figure 1.8, this condition can only be satisfied if the dielectric function of the nanoshell has a negative real component at optical frequencies (as a material with a dielectric function of zero is not physically realizable). From Figure 1.6, it is apparent that gold satisfies this condition – which explains why gold nanoshells exhibit LSPR at optical frequencies. Notably, these conditions also hold for other metal nanoparticles at different frequencies, such as silver and copper nanospheres, which have been synthesized [24]. The behavior of gold nanoshells cannot be reproduced for macroscopic gold shells at longer wavelengths by simply invoking the scale-invariance of Maxwell's equations. This is because of the frequency-dependence of gold's dielectric function [19].

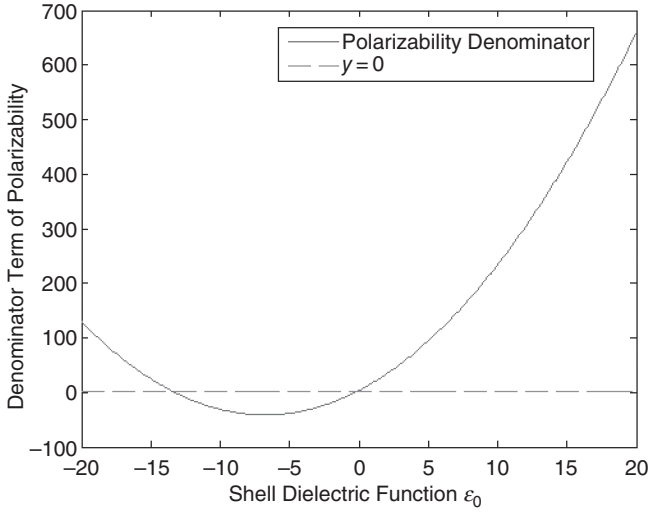

Figure 1.8 Resonance occurs for two dielectric function values. Only the negative value is physically realizable.

The value of the dipole approximation resides in its ability to produce good estimates for the absorption and scattering properties of nanoshells, including the position of the resonant extinction peak. From Mie scattering theory, the absorption σ_{abs} and scattering σ_{sca} cross-sections are given by [25]:

$$\sigma_{abs} = \frac{2\pi}{\lambda\varepsilon_o}\mathrm{Im}(\alpha) \quad \text{and} \quad \sigma_{sca} = \frac{8\pi^3}{3\varepsilon_o^2\lambda^4}|\alpha|^2,$$

so the absorption and scattering cross-sections are both functions of ω and λ. It is thus possible to plot the extinction cross-section $\sigma_{ext} = \sigma_{abs} + \sigma_{sca}$ to determine the position of the plasmon resonance peak (Figure 1.9).

Although the quasi-static approximation provides a relatively good estimate for the position of the resonant extinction peak, it drastically underestimates the plasmon linewidth of the observed extinction peak. Whereas, the full-width, half-maximum of the observed peak is ~300 nm, the linewidth of the approximated peak is less than 100 nm, giving an artificially sharp resonance. The broadness of the plasmon linewidth comes from three major sources [26]: (i) unavoidable polydispersivity; (ii) deviations between the *true* dielectric function of the gold shell and the bulk dielectric function of gold; and (iii) contributions from quadrapole and higher-order multipole resonances. It will be shown here how the first two can easily be incorporated into the quasi-static approximation.

Due to the nature of their synthesis in solution, nanoshells are not perfectly uniform spheres; rather, they generally exhibit size distributions of ±5–20% (standard deviation) [13, 17, 26–28]. As a result, the resonance peak becomes a weighted average of the contributions from the resonance peaks' individual nanoshells. The

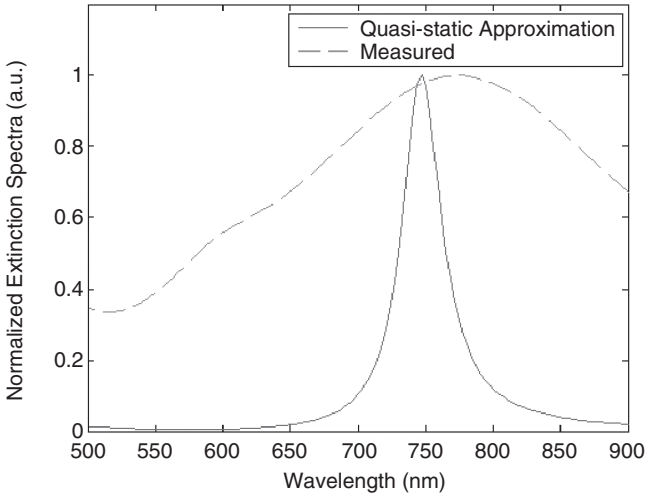

Figure 1.9 Comparison between the quasi-static approximated and measured resonant extinction peaks for gold nanoshells with nominal core radius of 58 nm and shell radius of 75 nm. The extinction peak was measured from nanoshells in deionized water with a Beckman Coulter DU 720 spectrophotometer.

second broadening mechanism arises from the nature of the dielectric function of the gold shell. The mean free electron scattering path in gold is ~42 nm, which is typically greater than the thickness of the thin shell, so the bulk gold dielectric function must be modified to account for electron scattering at the gold interface. Electron scattering reduces electron phase coherence, leading to broadening [13]. The effect of electron scattering is accounted for in the dielectric function by using the modified bulk collision frequency

$$\Gamma_{gold\ shell} = \Gamma_{bulk} + A\nu_f / a$$

with Fermi velocity $\nu_f = 1.4 \times 10^6\,\mathrm{m\,s^{-1}}$, shell thickness a and geometric parameter A, which is generally between 1–5 for nanoshells, depending on their exact dimensions. When these corrections are implemented into the approximation, there is a much better agreement (Figure 1.10). The electron-scattering correction also explains the origin of the absorption/scattering ratio tunability. As shown in Figure 1.11, the increased energy dissipation (absorption) in a small nanoshell is accounted for classically by an increase in the imaginary component of the shell's dielectric function.

In order to account for the third source of error, which exists because the electric field varies over the spatial extent of the nanoshell, the quasi-static approximation must be abandoned in favor of more rigorous analytical approaches.

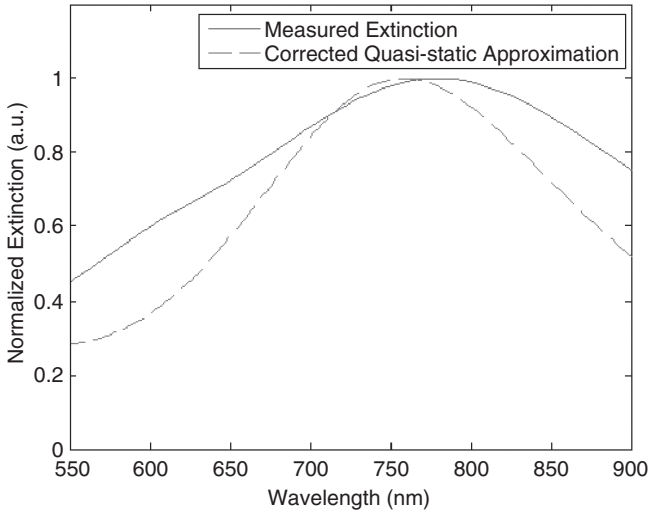

Figure 1.10 By implementing corrections for electron scattering and polydispersivity (normal distribution with standard deviation of ±15%), there is much better agreement between the approximation and experimental extinction spectra for nanoshells with inner radius of 58 nm and outer radius of 75 nm.

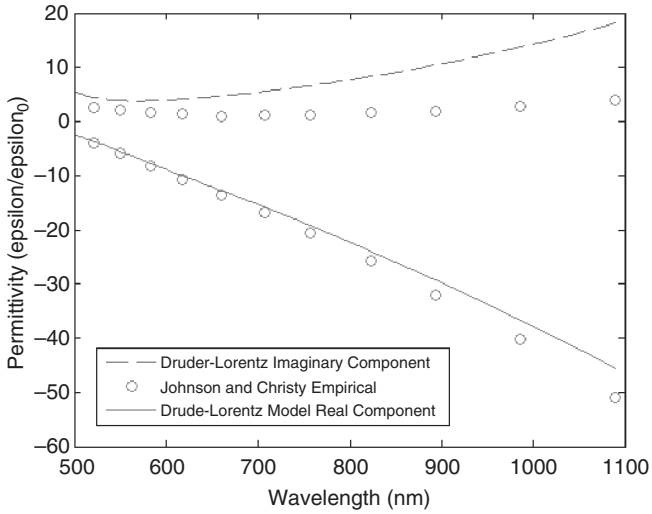

Figure 1.11 Corrected dielectric function for a small gold nanoshell with an inner radius of 20 nm and outer radius 25 nm. For thin nanoshells, the imaginary component of the dielectric function increases significantly, leading to greater absorption.

1.2.2.3 Mie Theory

Mie scattering theory [29, 30] provides complete analytical solutions of Maxwell's equations for the scattering of electromagnetic radiation by particles with spherical or cylindrical symmetry. A full treatment of scattering from concentric spherical shells was published by Aden and Kerker in 1951 [30]. In Mie theory, the harmonically oscillating electromagnetic fields are expressed in terms of a set of spherical vector basis functions, so that each term in the expansion represents one of the resonances. The first term in the expansion is the dipole term, as represented by the quasi-static approximation. Mie theory is a versatile technique for determining the optical properties of nanoshells or any other spherical particles of any dimension. Mie codes for Matlab and other mathematical software are available online. Christian Matzler's code (available online at: http://www.iwt-bremen.de/vt/laser/wriedt/Mie_Type_Codes/body_mie_type_codes.html) is particularly easy to use as it calculates scattering, absorption and phase functions for solid spheres and spherical shells. In general, Mie theory does an excellent job of predicting the far-field optical properties of gold nanoshells [27].

1.2.2.3.1 **The Plasmon Resonance Hybridization Picture** Although the plasmon resonance tunability of nanoshells is predicted from Mie theory calculations (see Figure 1.3), Mie theory does not intuitively explain why the position of the plasmon resonance peak can be selected by adjusting the core/shell ratio. In order to account for the nanoscopic origin of their tunability, the plasmon hybridization picture must be invoked [21]. It must be noted that the analysis is restricted to the dipole limit, as defined previously. A more rigorous hybridization analysis, which takes higher-order multipoles into account has not been published. In the hybridization picture, the geometry-dependent nature of plasmon resonance in a nanoshell results from the interaction of individual sphere and cavity plasmons. The strength of interaction depends on the thickness of the gold shell, and hence the core/shell ratio. The frequencies of the bonding (ω_-) and anti-bonding (ω_+) plasmon modes decomposed as spherical harmonics of order l are given by

$$\omega_{l\pm}^2 = \frac{\omega_B^2}{2}\left[1 \pm \frac{1}{2l+1}\sqrt{1+4l(l+1)\left(\frac{r_1}{r_2}\right)^{2l+1}}\right]$$

where ω_B is the bulk plasmon frequency. For bonding plasmon modes, an increased core/shell ratio produces lower-frequency plasmon modes, corresponding to plasmon resonance at longer wavelengths, which is consistent with Mie theory calculations.

1.2.2.4 Near-Field Enhancement

Near-field enhancement occurs because large amounts of charge temporarily build up on the surface of a gold nanoshell exposed to light at resonant wavelengths. A physically intuitive way to understand the phenomenon of local near-field enhancement is to imagine a plane wave incident upon a nanoshell [31]. Because of the nanoshell's high extinction cross-section, light from a large swath of area interacts

with the nanoshell. As predicted by the quasi-static approximation, the electric field surrounding the nanoshell then appears as an enhanced or 'concentrated' dipole field, which oscillates at the driving frequency of the incident electromagnetic field. In this framework, the nanoshell can also be viewed as a nano-antenna [17].

1.2.2.5 **Photoluminescence**

The enhanced photoluminescent properties of gold nanoshells and gold nanorods are mediated by LSPR [32]. Quantum mechanically, luminescence arises from radiative recombination of electron-hole pairs at selected symmetry points in the Brillouin zone [33]. Visible photoluminescence results from radiative recombination of electron-hole pairs formed by *interband* transitions in which electrons are excited from the d-band to the sp-conduction band. On the other hand, NIR luminescence results from the radiative recombination of electron-hole pairs formed by lower-energy *intraband* transitions within conduction states below the Fermi surface [32]. Whereas, Mooradian [34] reported luminescence from smooth gold films with small quantum efficiencies of ~10^{-10}, quantum efficiencies over a million times greater (10^{-3}–10^{-4}) have been observed in gold nanorods [35], and similar increases have been observed in gold nanoshells [1].

This enhanced luminescence results from localized surface plasmons [32, 33]. Surface plasmons produce transient, high charge densities near the surface of gold nanoshells and nanorods, leading to localized strong electric fields and, in turn, strong field gradients. The presence of strong field gradients enables transitions which would, ordinarily, be dipole-forbidden. Additionally, such fields have large associated wavenumbers, which carry enough momentum to allow direct intraband transitions within the conduction band. Localized surface plasmons enable the energy from these transitions to radiatively decay into the far field [32].

1.2.3
Photo-Thermal Material Characteristics

The highly efficient coupling of nanoshells to incident electromagnetic energy at surface plasmon frequencies leads to intense absorption and, in turn, heating of the nanoshells. Clarke *et al*. have monitored the thermal profile of individual nanoshells embedded in a dried lipid layer placed in an aqueous medium [36]. Under NIR excitation, the nanoshells triggered a lipid phase transition (24 °C), which induced local liposome budding. In general, nanoshells exhibit excellent thermal stability, in that their structure remains intact when exposed to light intensities required for applications in imaging and photothermal therapy. However, nanoshells are susceptible to photo-thermal damage (deformation and destruction) when exposed to very high incident intensities (fluence rates). A review of the literature reveals wide variations in the measured damage thresholds dependent on experimental conditions.

Park *et al*. investigated the damage threshold of gold nanoshells (800 nm resonance) in the context of two photon imaging studies [1]. Nanoshells in solution

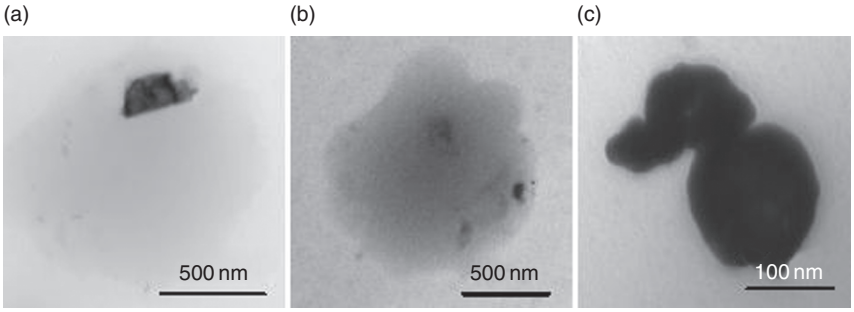

Figure 1.12 Images of nanoshells destroyed by laser irradiation. Gold (panels a and c) from the outer shell and silica from the core (panel b) [1].

remained intact when exposed to multiple Ti:sapphire 300 fs laser pulses at an average fluence rate of $9.06 \times 10^5\,W\,cm^{-2}$. However, when the fluence rate was increased by a factor of three to $2.71 \times 10^6\,W\,cm^{-2}$, the nanoshells were damaged, as observed in TEM images (Figure 1.12). Importantly, the laser fluence rates required for two photon imaging ($0.8–5 \times 10^5\,W\,cm^{-2}$) were significantly below the damage threshold.

Aguirre *et al.* performed damage threshold experiments on two sets of nanoshells for single pulses, providing insight into the mechanisms responsible for nanoshell damage [37]. Nanoshells resonant at 800 nm were placed in a rotating quartz cell and irradiated with a Ti:sapphire laser at a repetition rate of 250 kHz and pulse duration of 300 fs. Under these conditions, each nanoshell is exposed to one pulse on average. A separate group of nanoshells resonant at 1064 nm were placed in a small cuvette and irradiated with a single 9 ns pulse from a Nd:Yag laser. The damage mechanism and threshold were found to depend on the energy and pulse duration.

For the 9 ns pulse, complete destruction resulted primarily from photofragmentation and was only observed for energies of at least 0.005 mJ (average pulse fluence rate = $7.86 \times 10^3\,W\,cm^{-2}$). It has been posited that photofragmentation arises from an extreme photoelectric effect [38]. Energetic laser pulses cause electrons to be ejected from the gold shell, leaving excess positive charge, which causes the shell to explode due to coulombic repulsion.

For the 300 fs pulse, energies greater than 1.2 μJ (average pulse fluence rate = $9.52 \times 10^{10}\,W\,cm^{-2}$) resulted in the melting of nanoshells. The amount of energy absorbed from a 1.2 μJ pulse correlates with a lattice temperature of 1064 °C, which is the melting point of bulk gold. Much lower energies are required to destroy nanoshells under femtosecond pulses than nanosecond pulses because heat diffusion to the surroundings is limited in the femtosecond time regime. Single-pulse energies below 1.2 μJ did not produce melting; however, similar to Park *et al.*, multiple pulses were found to produce a slow reshaping and eventual degradation of the nanoshell structure, which is explained by large temperature rises near defects in the polycrystalline structure of the gold shell.

Of critical importance is the fact that the radiant intensities required to damage gold nanoshells are many orders of magnitude greater than those encountered in most applications. For instance, when nanoshells are used to mediate photothermal therapy, incident intensities are only in the $10\,W\,cm^{-2}$ range [4, 39].

1.3 Synthesis and Bioconjugation

1.3.1 Synthesis

Silica-core gold nanoshells, 'a new frequency-agile nanoparticle', were first fabricated by Oldenburg, Averitt, Westcott and Halas of Rice University, as described in their 1998 publication, *Nanoengineering of Optical Resonances* [40]. The theory predicting the plasmon resonance-derived optical properties of gold nanoshells had been laid out by Neeves and Birnboim [41] of the Rensselaer Polytechnic Institute in 1989, and further explored by Haus *et al.* in 1992 [28]. Members of the Halas group now hold several patents related to their pioneering work with nanoshells [42–45]. In this section we describe the synthesis of gold nanoshells employed by Oldenburg *et al.*, along with various techniques for functionalizing their surfaces. A detailed step-by-step synthesis protocol has been provided by Pham *et al.* [46]. The dimensions of the nanoshells (core radius and shell thickness) are controlled by varying the reactant concentrations.

The original synthesis is a four-step process [40] in which first, monodisperse silica nanoparticles are grown using the Stober method to produce the spherical dielectric cores [47]. The Stober method produces spherical silica particles by means of hydrolysis of alkyl silicates and subsequent condensation of silicic acid in alcoholic solution with an ammonia catalyst. In the second step, the surface of the silica nanoparticles is functionalized by the adsorption of an organosilane (3-aminopropyltriethoxysilane), with its amine tails protruding from the surface. In the third step a solution of gold colloid (~1–2 nm in diameter) is added to the solution. The gold colloid is produced separately from reduction of $HAuCl_4$ by alkaline tetrakis(hydroxymethyl)-phosphonium chloride, according to the method of Duff [48]. The gold particles bond to the organosilane linker via the amine group, producing silica nanoparticles with a smattered, uneven gold coating [49]. A final reduction process is used to produce silica nanoparticles with a uniform layer of gold – that is, a gold nanoshell. In the reduction process, the 'seeded' gold particles which are covalently bonded to the silica core serve as nucleation sites where an aged mixture of chloroauric acid and potassium carbonate is reduced in solution in the presence of sodium borohydride. This process forms a highly crystallized gold shell through Oswald ripening [50]. Transmission electron microscopy (TEM) images of the nanoshells during different phases of growth are shown in Figure 1.13.

UV-visible spectroscopy is used to monitor reaction kinetics, whereby complete nanoshell growth is confirmed by the appearance of characteristic plasmon extinc-

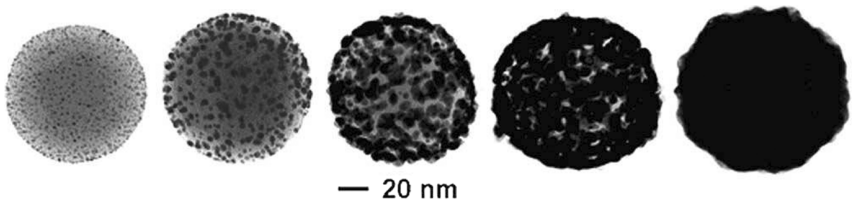

Figure 1.13 Transmission electron microscopy images of nanoshell growth phases from silica core (left) to gold-covered nanoshell (right) [39].

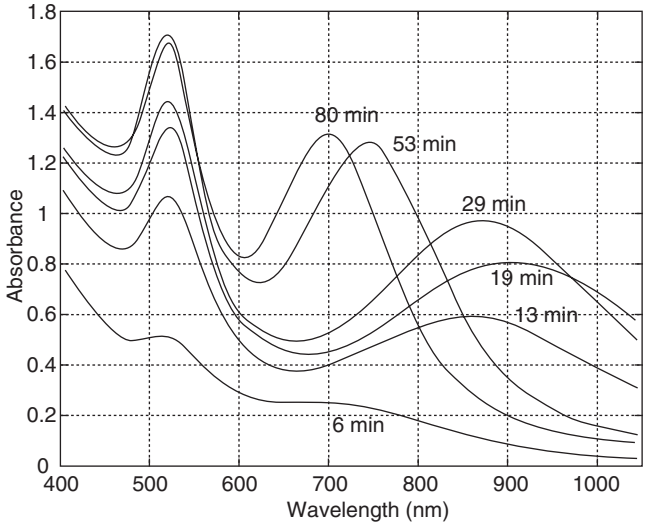

Figure 1.14 Ultra-violet/visible absorption spectrum for Au/Au_2S gold nanoshells as growth proceeds [40].

tion peaks (Figure 1.14). When using this method, the polydispersity (standard deviation) of nanoshells is generally close to 10% [40]. Recently, Phonthammachai *et al.* have published an alternative method for nanoshell synthesis, which employs the deposition–precipitation method [51]. The ideal reaction conditions are detailed thoroughly, including optimal pH, reaction temperature, reaction time and reactant concentrations. This method appears to be equally robust and more cost-effective than the original synthesis.

When the nanoshells have been fabricated it is possible to alter their surface topography through chemical postfabrication texturing. Wang *et al.* have reported site-selective chemical etching of nanoshells by exposing them in solution to the alkanethiol molecule, cystamine [52]. Such etching dramatically increases the roughness of the nanoshell surface, and leads to the production of 'hot spots' [32] where the near-field is predicted to be enhanced by a factor of 30 or more. Wang

et al. confirmed some degree of near-field enhancement by performing surface-enhanced Raman scattering (SERS) experiments, where increased signal intensities were observed for chemically etched nanoshells [52].

1.3.2 Bioconjugation: Smarter Nanoshells

The biologically inert gold surface of nanoshells [53] facilitates bioconjugation with antibodies and other biomarkers, rendering nanoshells capable of selectively binding to *in vivo* targets [54, 55]. The following examples of successful bioconjugation schemes should provide a general idea of the chemistry involved in the production of bioconjugated nanoparticles.

Sokolov *et al*. have synthesized bioconjugates of gold nanospheres with monoclonal antibodies against epidermal growth factor receptor (EGFR), a transmembrane glycoprotein (M_r 170 000) which is overexpressed in cancers originating from epithelial cells [55]. Colloidal gold of various sizes is prepared using a citrate reduction of $HAuCl_4$ (a detailed description of the protocol can be found in Ref. [56]). To prepare the bioconjugates, the gold colloid is diluted with 20 m*M* HEPES buffer, and anti-EGFR monoclonal antibodies are reconstituted in the same buffer at 100 μg ml^{-1} and mixed at a 1:1 volume ratio and allowed to interact for 20 min at room temperature. In this environment, gold nanospheres bind noncovalently with anti-EGFR antibodies at their isoelectric point to form stable bioconjugates. Polyethylene glycol (PEG) is added to the solution up to a final concentration of 0.2 mg ml^{-1}, after which the solution is centrifuged to remove any unbound antibody. After a second wash, the anti-EGFR gold nanoparticle pellet is resuspended in phosphate-buffered saline (PBS).

Human epidermal growth factor receptor 2 (HER2) is a frequently used breast cancer biomarker, and Loo *et al*. have successfully bioconjugated gold nanoshells with HER2 antibodies to target human mammary adenocarcinoma cells *in vitro* [54]. In the synthesis, *ortho*-pyridyl-disulfide-*n*-hydroxysuccinimide–PEG polymer (OPSS) is used to tether the antibodies on the surface after which, using $NaHCO_3$ (100 m*M*, pH 8.5), the OPSS is resuspended in a volume equal to that of the HER2 antibodies. The reaction bonding OPSS to anti-HER2 proceeds on ice for about 12 h, after which any excess OPSS is removed via membrane dialysis. The antibody complex (0.67 mg ml^{-1}) is then allowed to interact with added gold nanoshells (~10^9 nanoshells ml^{-1}) for 1 h, and any unbound antibody is then removed by centrifugation. The functionalized gold nanoshells pellet is then resuspended in potassium carbonate solution (2 m*M*). Following antibody conjugation, the nanoshell surfaces are further modified with PEG-thiol to prevent any nonspecific adsorption and improve biocompatibility.

Recently, Kumar *et al*. published a complete protocol for conjugating antibodies onto the surface of gold nanoparticles in a highly efficient manner [57]. This novel conjugation strategy employs a heterofunctional linker, hydrazide–PEG–dithiol, to directionally attach the nonbinding (Fc) region of the antibody to the gold surface. This technique enjoys several significant advantages over standard adsorption

techniques; mainly that the binding orientation of the antibodies is controlled to ensure maximum functionality and, due to the binding specificity, less antibody is required.

Bioconjugation dramatically enhances the clinical prospects of gold nanoshells by rendering them capable of targeting specific tissues through molecular recognition. Undoubtedly, innovative conjugation strategies will play an increasingly important role in the development of gold nanoshells for targeted therapeutics and diagnostics. In the next section, the connection between bioconjugation and biodistribution will be explored.

1.4 Biodistribution, Toxicity Profile and Transport

The dynamic biodistribution of nanoshells *in vivo* is of considerable clinical interest. Optimal imaging and treatment strategies require achievement of the highest concentration of nanoshells in the target tissue (i.e., a solid tumor), while minimizing concentrations in surrounding healthy tissues. Knowledge of the quantity of nanoshells reaching the target volume is needed to ensure optimal dosing.

Ultimately, the *in vivo* transport of nanoshells arises from a complex milieu of physical (pressure gradients, passage through vascular perforations, diffusion), chemical (antibody binding, transient binding) and cellular (endocytosis, vacuolar transport) processes [58]. A number of *in vivo* studies have been carried out to examine the net effect of transport, the differential and time-dependent distribution of nanoshells in various physiological compartments, namely the targeted tumor, blood, muscle tissue and major organs [59–62]. To date, the vast majority of *in vivo* studies have employed a murine model, whereby nanoshells are delivered intravenously through the tail vein and enter the systemic circulation. The biodistribution in human patients can likely be predicted based on existing pharmacokinetic modeling techniques, which use well-defined scale-up laws to estimate transport parameters [63].

In general, the distribution of nanoshells depends strongly on whether passive or active targeting methods are employed. Passive targeting relies exclusively on the nanoshell's size and a tumor's inherently 'leaky' vasculature to produce accumulation at tumor sites through an enhanced permeability and retention (EPR) effect [64]. In active targeting, the nanoshell's surface is functionalized with antibodies or other biomolecules, which bind to surface receptors on malignant cells to produce an enhanced accumulation at the tumor site [65]. Both targeting mechanisms are hindered by intrinsic host immune mechanisms, which clear nanoshells from circulation [66]. In both cases, the total circulation time is believed to correlate strongly with accumulation at the tumor site, independent of other anatomical and physiological factors [67]. The surface of gold nanoparticles is now routinely functionalized with PEG (PEGylation) to 'stealth' the nanoparticles from immune surveillance, and this has led to a dramatic increase in circulation times [68].

The following discussion is divided into three parts. First, an overview is provided of the techniques used to quantify the dynamic biodistribution of nanoshells, and the corresponding results. Second, the individual transport mechanisms responsible for the observed biodistribution are explored, based on information obtained from studies examining the transport mechanisms of similar-sized particles. Third, an overview is provided of the benign toxicity profile of nanoshells.

1.4.1 Biodistribution Studies

The current 'gold standard' for quantifying nanoshell concentrations in tissue is neutron activation analysis (NAA) [59]. This method requires the tissue excision, dehydration and bombardment of the sample of interest with neutrons in a nuclear reactor. Gold nanoshells absorb the neutrons, undergo a nuclear transition, and emit gamma rays with energies that are characteristic of gold. These gamma rays are then detected and related to the quantity of nanoshells present in the sample. James *et al*. employed this method to measure the concentration of nanoshells (~120 nm diameter) in different organs in mice at various time points [59]. Female albino mice with subcutaneous tumors (~5 mm) were injected with 100 µl of an isotonic saline solution of PEGylated nanoshells (2.4×10^{11} nanoshells ml^{-1}, passive targeting) and sacrificed at 1, 4, 24 and 48 h. Blood, liver, lung, spleen, muscle, kidney, bone and brain tissues were then analyzed using NAA. The study yielded several key findings; namely that tumor concentrations peaked at 24 h after injection, and the total tumor accumulation represented approximately 1% of the administered dose. Tumor concentrations were elevated relative to the blood, lungs, brain, bone and kidneys. (Figure 1.15) However, the highest accumulations were found in the liver and spleen, due to involvement of the reticuloendothelial system (RES).

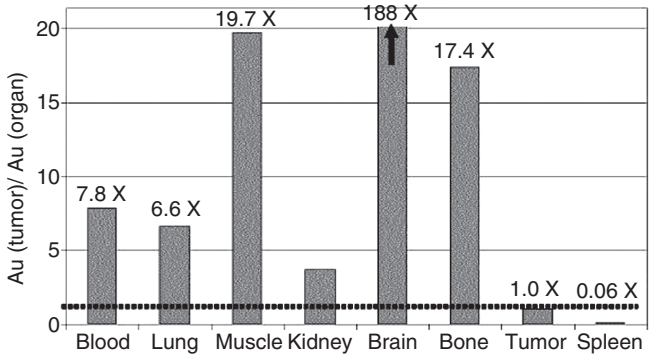

Figure 1.15 Ratio of tumor to organ concentrations at 24 h after dosing. Very high concentrations are observed in the spleen due to the action of the reticuloendothelial system [59].

Although this study provides valuable information regarding the biodistribution of nanoshells in mice, it does not address the question of how nanoshell size might affect biodistribution. Recently, De Jong *et al.* demonstrated the size-dependent nature of gold nanosphere organ distribution in normal, tumor-free rats using inductively coupled plasma mass spectrometry (ICP-MS) [69]. Rats were injected intravenously with nanospheres with diameters of 10, 50, 100 and 250 nm, respectively, and then sacrificed 24 h after injection. For all sizes of nanospheres, the highest concentrations were found in the blood, liver and spleen. However, there was a clear difference between the smaller (10 nm) and the larger nanospheres, with the smaller particles exhibiting a more pervasive organ distribution and being the only particles with detectable accumulations in the brain. Of particular interest was the fact that the NAA data for 120 nm gold nanoshells and the ICP-MS data for 100 nm nanospheres were not in good agreement. After 24 h, James *et al.* found the concentration of nanoshells in the spleen to be about fivefold greater than in the liver (1890 versus 311 $\mu g\,g^{-1}$), whereas De Jong *et al.* found higher concentrations of nanospheres in the liver than the spleen (3268 versus 1793 $ng\,g^{-1}$). This very significant discrepancy warrants further investigation, since it does not eliminate the possibility that there might be substantial differences in the biodistribution of gold nanospheres and nanoshells.

While generally providing excellent accuracy, NAA and ICP-MS have several drawbacks. Both techniques are labor-intensive, take significant time to acquire results, and are incapable of *in vivo* quantification because the organism must be sacrificed. In contrast, diffuse optical spectroscopy (DOS) and dynamic light scattering (DLS) provide a rapid means for determining *in vivo* nanoshell concentrations noninvasively. In DOS, a probe containing both optical source and detector fibers is placed in direct contact with the tissue [60], and the diffusely reflected light is then collected and spectrally analyzed. The concentration of nanoshells can be measured by fitting the diffusely reflected spectrum to a diffusion model through nonlinear regression. Zaman *et al.* used DOS to quantify nanoshell concentrations in live mice, yielding values within 12.6% of the known concentrations. DOS provides reliable average concentration measurements in the volume sampled, but can only be used to sample regions accessible by the probe.

Xie *et al.* have used DLS to quantify nanoshell concentrations in whole blood [61]. Blood samples (15 µl) were taken from mice at fixed times after nanoshell injection to study the circulation times and clearance in blood. DLS estimates particle concentrations by comparing the relative scattering from particles of a given size to particles of a known concentration and different size. In this study (where the comparative scatterer was Triton X-100 micelles), the measured whole-blood values were in good agreement with NAA measurements, showing an exponential decay of blood concentrations with a half-life of 5 h.

For malignancies located in close proximity to the surface of the epithelium, optimal biodistribution may be achieved through topical delivery rather than systemic administration. Although the results of *in vivo* studies have yet to be published, *in vitro* studies have yielded promising results. Using engineered tissue

constructs, Sokolov *et al*. showed that gold nanospheres (~12 nm diameter) can be delivered throughout the epithelium by using the penetration enhancers polyvinylpyrollidone (PVP) and dimethyl sulfoxide (DMSO), both which have been approved by the FDA for use in humans [55]. Confocal reflectance microscopy measurements revealed a uniform distribution of nanoshells up to a depth of 400 μm, which is significant because precancers of the squamous epithelium typically originate at a depth of 300–500 μm below the surface.

A study comparing the effects of active and passive targeting on the biodistribution of gold nanoshells has not been carried out to date. However, Qian *et al*. have conducted a similar study using gold nanospheres (~80 nm diameter), which demonstrated the advantage of employing active targeting mechanisms [65]. Nanoparticle concentrations were measured in sacrificed mice with xenografted human squamous carcinoma tumors, using ICP-MS. For active targeting, the nanoparticles were conjugated to anti-EGFR antibodies that bind to the EGFR, which is normally overexpressed on the surface of tumor cells. The targeted gold nanoparticles were found to accumulate in the tumor 10-fold more efficiently than the nontargeted particles, which represented a substantial difference. It is therefore likely that enhanced accumulations would be observed with targeted nanoshells.

The effects of active targeting have also been studied on the cellular level. For example, Fu *et al*. used polarized light scattering to quantify the number of antibody-conjugated nanoshells bound to a targeted cancer cell [70]. Here, SK-BR-3 breast cancer cells were incubated with anti-HER2/nanoshell bioconjugates in a cell culture, with approximately 800–1600 nanoshells being bound to the HER2 receptors on each cell. Cell-specific anti-HER2 conjugates were shown to exhibit binding efficiencies more than 10-fold greater than those of nonspecific anti-IgG conjugates. Clearly, active targeting mechanisms will play an increasingly important role in determining the maximum therapeutic efficacy of nanoshells for the treatment of various cancers.

1.4.2 Transport Mechanisms

The transport of molecules and particles in solid tumors is a vast and active area of research because if its potential to illuminate new methods for achieving optimal delivery of therapeutic agents to the tumor site. The following discussion is intended only as an overview of the subject area, outlining the basic characteristics and underlying mechanisms of nanoparticle transport in solid tumors, which can be generalized to nanoshells.

Upon introduction into the host's vasculature, the fate of a typical nanoshell is predictable if the host is tumor-free and the nanoshell surface is not modified by antibodies or other protein-binding ligands. As normal blood vessels are highly impermeable to particles the size of nanoshells [58, 62], the nanoshells will remain in circulation until they reach the spleen and liver, where they are scavenged by macrophages, such as Kupffer cells, in the host's RES (this accounts for the high

concentrations observed in the liver and spleen). Large numbers of nanoshells remain in the RES tissues for many weeks and perhaps longer [59]. However, conflicting data exist with regards to the eventual clearance of nanoshells. Whereas, gold nanoparticles smaller than 10 nm are slowly eliminated from the host's system via renal excretion [66], the case may be different for larger gold nanoparticles. In magnetic resonance imaging (MRI) studies, Choyke *et al.* found that 'virtually no' contrast agents (gadolinium dendrimers) larger than 11 nm were eliminated through renal excretion [71]; hence, it stands to reason that whole gold nanoshells (~100 nm) would also be excluded from renal clearance. However, significant amounts of gold and copper have been found in the urine of mice injected with gold-copper nanoshells, which suggests partial renal clearance [72]. Nanoshells are also likely excreted in the feces, similar to quantum dots [73].

If a tumor is present, then the transport and biodistribution of nanoshells changes significantly. The tumor vasculature is physiologically distinct from normal vasculature, as it lacks a functional lymphatic system [74], exhibits spatial and temporal heterogeneity [58], structural irregularity, abnormal fluid flow, and hyperpermeability to particles with diameters up to 1.2 μm [75]. The overall result is a series of peculiar transport properties that vary across the tumor type, stage of development and the surrounding microenvironment [67].

One prominent feature of vascular transport in tumors is the EPR effect [64], whereby particles with diameters of tens to hundreds of nanometers extravasate through the 'leaky' microvasculature and accumulate in the tumor interstitium. For example, a 400–600 nm cut-off has been found for the extravasation of liposomes [76]. Multiple causes of associated tumor 'leakiness' have been identified, including physical openings, cytokine-influenced permeability changes and various cellular transport mechanisms. Hashizume *et al.* showed that, in highly leaky MCa-IV mouse mammary tumors, 14% of the vessel surface was lined with poorly connected, overlapping endothelial cells. Transcellular holes were also present, but these were only 8% as numerous as intercellular openings [75]. An electron microscopy image showing an open endothelial gap in a tumor blood vessel in a liposome-injected mouse is shown in Figure 1.16, where the liposomes can be seen migrating through the open junction.

Dvorak *et al.* investigated extravasation with fluorescence and electron microscopy by injecting tumor-bearing mice and guinea pigs with fluoresceinated dextrans (diameters of 2.4, 11.6 and 17.4 nm) and colloidal carbon (~50 nm) [62]. (Note: it very worthwhile viewing the images produced in this study because they provide an excellent visual description of tumor vessel architecture and morphology.) The 11.6 nm and 17.4 nm tracers did not perfuse into normal tissues, but leaked extensively at tumor sites, thus setting a rough limit on the minimum size needed for nanoparticles to achieve preferential tumor accumulation. Additionally, colloidal carbon was found in vacuoles of individual tumor endothelial cells, thus implicating transcytosis as a mechanism for vascular transport and corroborating previous findings [77]. Cytokines also play an important role in extravasation. One peptide which is commonly secreted by human and animal tumors, namely vascular permeability factor (VPF), greatly enhances the permeability of nanoparticles

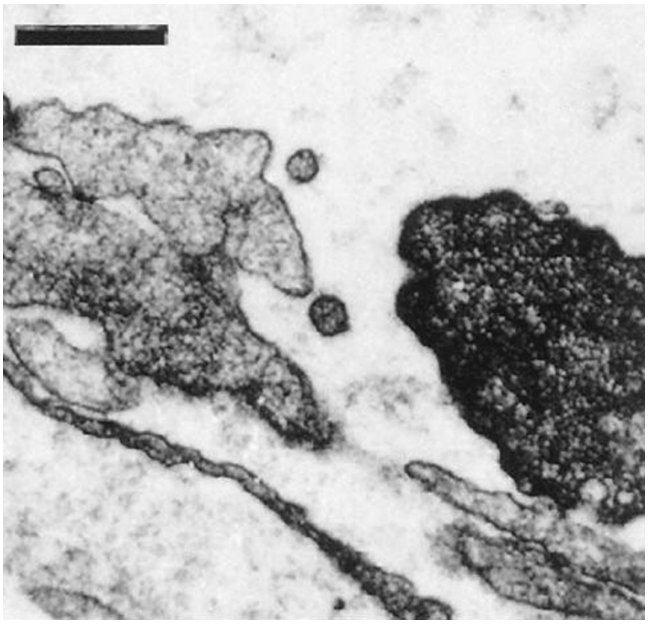

Figure 1.16 Endothelial gap with migrating liposomes. Two circular liposomes are seen crossing the gap.

[62]. For example, Monsky *et al*. demonstrated that low doses of vascular endothelial growth factor (VEGF) (10 ng ml^{-1}) doubled the pore sizes and increased the frequency of 400 nm pores in human colon xenografts [78].

After extravasation into the interstitial space, the transport of particles occurs via two mechanisms – diffusion and convection – which in turn presents a challenge to nanoparticle delivery because both processes produce very slow particle migrations. This is evidenced by the fact that extravasated particles remain largely confined to the perivascular region of the interstitium. By using two-photon microscopy, Park *et al*. showed that extravasated nanoshells remained in close proximity to the tumor microvasculature in subcutaneous mouse colon carcinoma xenografts, as can be seen in the three-dimensional (3-D) visualization in Figure 1.17. Similar transport behaviors of nanoshells have been demonstrated in other studies [58, 74, 79, 80].

Li *et al*. used photoacoustic microscopy to image the passive accumulation of nanoshells in murine colon carcinoma tumors grown in BALB/c mice [79]. Nanoshells were found to accumulate heterogeneously in the tumor, characterized by high concentrations in the vascular-rich cortex and very low concentrations in the tumor core. These results correlated well with previous studies, which have shown drug delivery to tumor cores to be minimal because of several inherent tumor mechanisms [80].

The high interstitial pressure in the center of a tumor that inhibits the convectional flow of extravasated particles in the vascular-rich periphery is a consequence

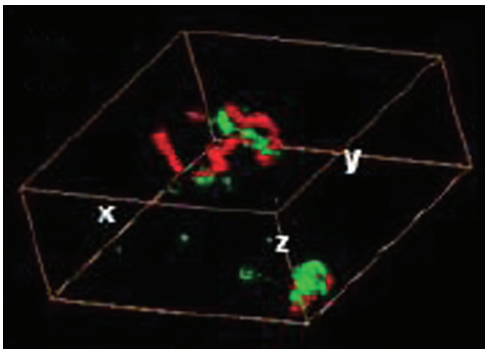

Figure 1.17 Nanoshells (green) in close proximity to tumor vasculature (red) [1].

of leakage from blood vessels, coupled with an impaired fluid clearance through dysfunctional lymphatic drainage [74]. Characteristically low diffusion coefficients hinder significant diffusion; for example, it has been estimated that it would take immunoglubulin G (IgG) several days to move 1 mm within a solid tumor, by the process of diffusion [58].

Transport also varies across tumor type, microenvironment and stage of development. For example, Hobbs *et al.* showed delivery to be less efficient in cranial tumors than in subcutaneous tumors, and that delivery was reduced during regression in hormone-dependent tumors during hormonal ablation [67].

Future research aimed at a better understanding of the mechanisms of transport, and how transport varies by tumor type, microenvironment and stage of development, will provide the valuable information required to optimize the therapeutic efficacy of gold nanoshells, gold nanoparticles and other cancer treatments.

1.4.3 Toxicity

Although no comprehensive studies evaluating the long-term (years) toxicity of gold nanoshells have yet been reported, all available evidence indicates that – at physiological doses – gold nanoshells are not cytotoxic and pose no short-term health risks. In fact, the favorable toxicity profile of nanoshells results from the nontoxicity of the shell components.

Gold has been used to treat rheumatoid arthritis since the 1930s [81], and is universally recognized as the most biologically inert of metals [81]. Likewise, silica nanospheres have been shown to be nontoxic in a murine mouse model [82]. The safety of gold nanospheres has been well documented; in experiments performed *in vitro*, gold nanospheres incubated with macrophages were found to be both noncytotoxic and nonimmunogenic [83]. Nanospheres were also found to reduce the production of both reactive oxygen species (ROS) and nitrite radicals, and did not stimulate the secretion of inflammatory cytokines.

Numerous *in vivo* studies conducted in mice have provided the best evidence that nanoshells are not only nontoxic but also safe. In all instances, mice treated with nanoshells exhibited no clinical abnormalities or side effects at months after treatment [4, 84, 85]. It should be noted that, although a prolonged respiratory exposure to high doses of crystalline silica has been linked to lung cancer in epidemiological studies [86], the carcinogenic potential of gold nanoshells is minimal for the following reasons. The silica used in nanoshells is completely obscured from the host by the gold shell, which is not carcinogenic. Likewise, comparatively lower doses of nanoshells would be necessary for clinical applications, and the intravenous route of administration prevents high concentrations from ever reaching the lungs. Although gold nanoshells can generally be considered 'safe', their long-term effects on human health will need to be closely monitored.

Significantly, gold nanoshells appear to be much safer than both quantum dots and gold nanorods. Quantum dots are, presumably, cytotoxic because the toxic heavy metals found in their cores (i.e., cadmium and lead) can leach into the surrounding environment [87]. The available evidence regarding the cytotoxicity of nanorods renders a split verdict, however, with some studies suggesting that nanorods have no effect on cell viability while others have demonstrated cytotoxicity. It should be noted that the cytotoxicity of nanorods appears to be solely related to the presence of cetyltrimethylammonium bromide (CTAB), a chemical used in their synthesis [72].

1.5 Biomedical Applications

Due to their unique physical characteristics and benign toxicity profile, gold nanoshells have been at the forefront of a growing number of biomedical applications. They have shown potential as integrated cancer targeting, imaging and therapy agents. As contrast agents, nanoshell bioconjugates have been used to detect and image individual cancer cells *in vitro* and in solid tumors *in vivo*. As photothermal agents, nanoshells have successfully been used in animal studies to induce thermal necrosis of tumors. On the laboratory bench, they have been used to potentiate thermal drug delivery in temperature-sensitive hydrogels. Outside the realm of cancer treatment, nanoshells have proven their worth in a number of novel applications; for example, as biosensors they have been used for the sensitive detection of biomarkers at the ng ml^{-1} level.

1.5.1 *In Vitro* Cancer Detection and Imaging

Detecting cancer in its earliest stages is strongly associated with positive patient outcomes, including reduced morbidity and improved five-year survival rates [88]. As many cancers originate from a small number of malignant epithelial cells [89], the ability to detect low numbers of malignant or precancerous epithelial cells

in vivo would represent a giant leap forward in the fight against cancer. Notably, it would facilitate the detection of cancer in its earliest stages, before any significant pathogenesis, tumor formation and metastasis. A number of groups have successfully demonstrated *in vitro* single cancer cell detection, with exceptional contrast and specificity, using bioconjugated gold nanoparticles as molecular-specific contrast agents. Here, the general detection scheme relies on conjugating nanoparticles to antibodies that target epithelial cell-surface receptors (e.g., EGFR and HER2) which are commonly overexpressed in cancer cells. The resultant high concentrations of nanoparticles found on the surface of targeted cancer cells, combined with their high scattering cross-sections, greatly facilitates imaging on the cellular level.

Loo *et al.* have used anti-HER2-conjugated nanoshells to detect and image HER2-positive SKBr3 breast adenocarcinoma cells using dark-field microscopy *in vitro* (Figure 1.18) [54, 90]. In this experiment, both SKBr3 and MCF7 (HER2-negative) cancer cells were incubated with nanoshells at a concentration of $8\,\mu g\,ml^{-1}$ for 1 h. Consequently, the SKBr3 cells targeted with molecular-specific anti-HER2 showed a marked (300%) increase in contrast over the nonspecific anti-IgG control group, whereas no appreciable differences in contrast were noted between HER2-negative control cell groups, indicating that nanoshells targeted the HER2 receptor on SKBr3 cells with high specificity.

Other types of gold nanoparticle, such as nanospheres and nanorods, have also been successfully employed to detect and image cancer cells *in vitro*. Durr *et al.* have used anti-EGFR-conjugated nanorods to detect and image A431 skin cancer cells embedded in a 3-D tissue scaffold using two-photon luminescence (TPL) microscopy [91]. The nanorods produced a TPL signal enhancement of more than three orders of magnitude over the intrinsic fluorescence of unlabeled cancer cells, which enabled the imaging of cancer cells up to a depth of 75 µm. El-Sayed *et al.* have used anti-EGFR gold nanorods to detect and image two oral squamous carcinoma cell lines, HSC 313 and HOC 3 [92, 93]. The nanorods were found to bind specifically and homogeneously to the surface of cancer cells with 600% greater

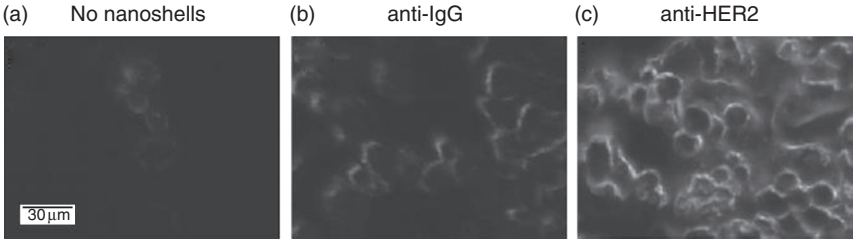

Figure 1.18 Dark-field images of SKBr3 cancer cells exposed to (a) no nanoshells, (b) anti-IgG-conjugated nanoshells and (c) anti-HER2 nanoshells. Note the significant difference in contrast between the anti-HER2 nanoshells designed to target breast cancer cells, and the control and anti-IgG nanoshells [54].

affinity than to nonmalignant cells. Dark-field microscopy revealed an intense resonant scattering from the labeled oral cancer cells, whereas scattering from a normal cell line (HaCaT) was minimal.

Sokolov *et al.* have used anti-EGFR-conjugated nanospheres and reflectance confocal microscopy to detect and image SiHa cervical cancer cells in 3-D tissue constructs [55], while Mallidi *et al.* used optoacoustic imaging in conjunction with anti-EGFR nanospheres to detect and image A431 skin cancer cells to depths of up 1 mm in tissue phantoms [94]. Optoacoustic imaging using nanoshells has been studied to a lesser extent [95]. Aaron *et al.* have used anti-EGFR gold nanospheres as molecular-specific probes to distinguish between normal and malignant cervical biopsies [89], with confocal reflectance images showing an up to a 21-fold difference in signal intensity between normal and abnormal biopsies. As an additional detection feature, a ~100 nm red shift in the reflectance spectra was observed in malignant biopsies; this was due to plasmon resonant coupling of aggregated nanospheres on the cell surface, where EGFR is densely expressed [96]. This feature also has a significant diagnostic value, as it provides a reliable quantitative assessment of tissue status. As a consequence of these findings, the use of gold nanoparticles for *in vitro* cancer detection and imaging is now well established.

1.5.2
In Vivo Detection and Imaging

Recently, progress in the detection and imaging of malignant cells *in vitro* has been followed up by *in vivo* studies, where bioconjugated gold nanoparticles have been used successfully to target and detect tumors in mice. Qian *et al.* have created specialized gold nanospheres for SERS imaging [65] that are first stabilized with PEG-thiol and then conjugated to a Raman reporter (malachite green) and to anti-EGFR antibodies for active tumor targeting. In the experiment, nude mice with xenografted human head and neck cancer tumors (Tu686) were injected with specialized nanospheres through the tail vein. The tumors were approximately 3 mm in diameter. After 5 h, NIR SERS spectra were obtained using a 785 nm excitation laser on a hand-held Raman system. The SERS spectra measured from an intramuscular tumor located ~1 cm below the surface were distinct from the background spectra, demonstrating the effective detection of small tumors at depths of at least 1 cm. However, based on a favorable signal-to-noise ratio, the authors concluded that the maximum achievable penetration depth for SERS detection was likely in the 1–2 cm range.

Aaron *et al.* have used anti-EGFR-conjugated nanospheres to monitor carcinogenesis *in vivo* in a hamster cheek pouch model [89]. A carcinogen, dimethylbenzanthracene (DMBA), was repeatedly applied to the hamster's inner cheek to induce carcinogenesis over the course of weeks. After anesthetizing the hamster, the inner cheek was then imaged with a portable confocal reflectance microscope before and after the topical application of gold nanospheres. The inner cheek was rinsed shortly after nanosphere application to eliminate any nonspecific binding.

Images were subsequently taken over the span of many weeks to detect and monitor dysplasia. At week zero, images taken before and after application were almost the same, but by week 3 there was a marked difference in the two images, indicating cancer progression and specific binding to cancer cells overexpressing EGFR. Although the results of this study highlighted the potential of gold nanoparticles for the localized optical detection of cancer cells *in vivo*, it should be noted that favorable results were not always repeatable. The authors of the study attributed such poor reproducibility to the thick keratin layer present in the buccal mucosa of hamsters, which inhibits nanosphere delivery.

Gobin *et al.* have demonstrated the role of nanoshells as contrast agents for *in vivo* optical coherence tomography (OCT) imaging [97]. BALBc mice with subcutaneous murine colon carcinoma tumors were injected with PEGylated nanoshells at 20 h before OCT imaging, which was carried out using a commercially available OCT system. Due to their large resonant scattering cross-sections and ability to accumulate at tumor site, the nanoshells were found to significantly enhance the optical contrast of the tumor compared to normal tissue. Thus, in nanoshell-treated mice the integrated scattering intensity was 56% greater in tumor tissue than normal tissue, whereas in control mice the difference was only 16%. It appears that gold nanoshells represent excellent contrast agents, and are suitable for a wide range of imaging techniques.

1.5.3
Integrated Cancer Imaging and Therapy Agents

Gold nanoshells and nanorods are not merely ideal agents for detecting and imaging cancer – the same nanoparticles can be used as therapeutic agents to treat cancer with photothermal therapy. Unlike nanospheres, nanoshells and nanorods can be engineered either to scatter NIR radiation for imaging, or to absorb it and efficiently convert it to heat for the selective destruction of targeted tumor cells. Nanoshells and nanorods are integrated multifunctional nanoparticles, useful for both imaging and therapy [90, 97]. Although the ability of both nanorods and nanoshells to mediate the photothermal destruction of targeted cancer cells *in vitro* has been established, until now only nanoshells have been shown to treat tumors effectively *in vivo*. However, the details of *in vivo* studies carried out with nanorods have not yet been reported.

1.5.4
In Vitro Studies

In an *in vitro* study, Hirsch *et al.* incubated breast carcinoma (SKBr3) cells with unconjugated nanoshells for 1 h, after which the cells were rinsed to remove unbound nanoshells and then exposed to 820 nm laser light with an intensity of $35\,W\,cm^{-2}$ for 7 min. After treatment, all nanoshell-treated cells within the laser spot were dead, whereas those cells in the control groups remained viable [4]. Others have carried out similar *in vitro* experiments. For example, Stern used

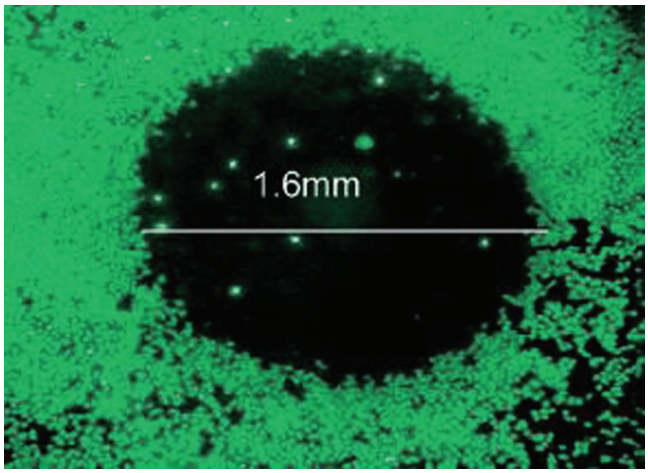

Figure 1.19 PC-3 prostatic cancer cells treated with gold nanoshells and exposed to NIR laser light focused to a spot size of 1.6 mm. Calcein viability staining reveals selective destruction of cells within the laser spot [98].

unconjugated nanoshells as mediators to photothermally ablate two types (PC-3 and C4-2) of human prostate cancer cell (Figure 1.19) [98], while Loo *et al.* used anti-HER2-conjugated nanoshells to target and ablate SKBr3 breast carcinoma cells [90]. In another study, El-Sayed *et al.* used anti-EGFR-conjugated gold nanorods to treat two human oral cancer cells types (HSC 313 and HOC 3) and a benign control, human epithelial keratinocytes (HaCat). After having exposed the cells to various intensities of 800 nm laser light for 4 min, irreversible photothermal injury of nanorod-treated cells was observed for intensities as low as 19 W cm^{-2}. More significantly, photothermal destruction was observed in malignant cells at less than half the laser power needed to induce destruction in healthy cells, thus permitting the selective destruction of cancer cells. Of particular interest here was the lower laser intensities needed to induce the destruction of malignant cells using nanorods compared to nanoshells. This presumably occurred because nanorods have a larger size-normalized absorption cross-section than do nanoshells [6]. An authoritative study evaluating the effectiveness of both types of nanoparticle under identical experimental conditions is yet to be published, however.

Everts *et al.* have conjugated gold nanospheres to adenovirus vectors to investigate their potential for combined photothermal and gene cancer therapy applications [99]. Adenovirus vectors, which normally do not infect cancer cells, were re-targeted to infect cancer cells expressing the tumor-associated oncoprotein carcinoembryonic antigen (CAE) *in vitro*, thus providing a method for introducing gold nanoparticles into the nuclei of targeted cancer cells. For *in vivo* applications, nanoshells or nanorods tuned to absorb in the NIR could be used to induce selective hyperthermia in particular segments in the genome of a tumor cell. However, more simple targeting mechanisms have been shown to be highly effective.

1.5.5 *In Vivo* Photothermal Therapy

Multiple *in vivo* studies have demonstrated the efficacy of nanoshells for the non-invasive treatment of tumors through targeted photothermal destruction [4, 84, 85]. Here, the overall concept is straightforward; nanoshells with absorption peaks in the NIR region of the spectrum (~800 nm) accumulate at the tumor site through passive and/or active mechanisms. The 800 nm absorption peak is in the NIR 'optical window' region of the spectrum where tissue absorption is minimal, permitting optimal penetration [15, 100]. When the tumor site is exposed to NIR radiation (which the nanoshells absorb intensely because of plasmon resonance), the absorbed energy is efficiently converted into heat, leading to thermal destruction of the tumor.

O'Neal *et al.* have successfully treated mice inoculated with tumors using this technique [84]. In the experiment, albino mice were inoculated subcutaneously with CT26.WT murine colon carcinoma cells in the right dorsal flank, and selected for treatment when the tumors had reached diameters of 3–5.5 mm. An aliquot (100 μl) of PEGylated nanoshell solution (2.4×10^{11} nanoshells ml^{-1}) was then injected via a tail vein. After allowing a 6 h period for the nanoshells to accumulate, the laser treatment was commenced, with the tumors being exposed to NIR light at 808 nm at 4 W cm^{-2} for 3 min. Measurements revealed a marked increase in surface temperature at the tumor site, to ~50 °C, and both tumor size and animal survival was monitored for up to 90 days after treatment. In the nanoshell treatment group, a complete resorption of tumors was observed within 10 days, and all mice were healthy and free of tumors at 90 days. By contrast, in the control groups the tumors continued to grow after sham treatment, with a mean survival time of 10.1 days (Figure 1.20). This dramatic difference in results highlighted the therapeutic potential of nanoshells.

In a separate study, Hirsch *et al.* studied the temperature distribution in tumors during thermal therapy, and highlighted the merits of injecting nanoshells directly into the tumor interstitium rather than administering them intravenously [4]. Female nonobese diabetic mice were inoculated with transmissible venereal tumor (TVT) cells in the hind leg, and the tumors allowed to grow until they reached a diameter of ~1 cm. Nanoshells were then injected interstitially to a depth of ~5 mm into the tumor volume. At only minutes (rather than hours) after injection, the tumor sites were exposed to NIR radiation (4 W cm^{-2}, spot diameter ~5 mm) for 6 min, during which the tumor volume temperatures were monitored using magnetic resonance temperature imaging. The mean change in temperature for the nanoshell group (37.4 ± 6.6 °C) was high enough to cause irreversible thermal damage, whereas the more modest temperature increase in the nanoshell-free control group (9.1 ± 4.7 °C) was insufficient to cause any permanent damage (Figure 1.21). Interestingly, the heating profile was approximately homogeneous, which indicated that the tumor volume contained a near-uniform distribution of nanoshells. The maximum temperatures were found approximately 1 mm below the surface, and not at the site of injection. Such behavior was most likely the

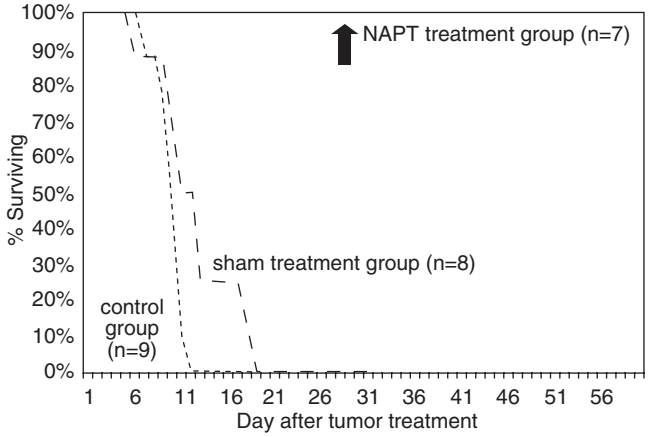

Figure 1.20 Survival rates of control, sham and treatment groups of mice undergoing nanoshell-assisted photothermal therapy (NAPT) of cancer [84]

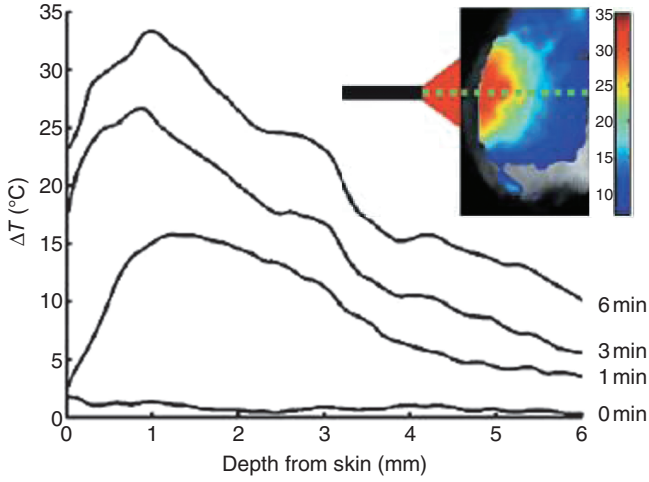

Figure 1.21 Net temperature change (°C) as a function of skin depth for various NIR exposure times [4].

result of higher photon fluence rates, which are known to peak slightly below the surface in highly scattering mediums, such as tissue [101]. An histological analysis performed after the procedure confirmed a diffuse distribution of nanoshells over a large volume within the tumor, and suggested that nanoshells might have a maximal therapeutic efficacy when administered directly to the tumor site.

Diagaradjane *et al.* have demonstrated that nanoshell-induced hyperthermia significantly enhances radiation therapy in mice [102]. In this study, mice with

xenografted tumors were injected with gold nanoshells via the tail vein and, at 24 h after injection, a NIR laser was used to induce hyperthermia at the tumor site for 3–5 min. Immediately hyperthermia induction, the mice received a single 10 Gy dose of radiation therapy. At 20 days after irradiation, the average tumor volume had more than doubled in the radiation cohort, but remained approximately constant in the combined hyperthermia/radiation cohort. The two mechanisms thought to account for the additional therapeutic benefit of hyperthermia are increased perfusion (which reduces the fraction of cells that contribute to radiation resistance) and a subsequent induction of vascular disruption, which causes extensive necrosis.

Stern *et al*. examined the dose-dependent nature of nanoshell therapy for treating prostatic cancer in a murine mouse model [85]. Surprisingly, a mere 20% modification in the administered dose was the difference between successful tumor ablation and continued tumor presence. In this study, male athymic nude mice were inoculated subcutaneously with PC-3 prostate cells in the hind flanks, and the tumors then grown until they attained a volume of approximately 40 mm^3. Nanoshells were then injected intravenously and NIR laser treatment commenced at 8 h after injection, so as to allow the nanoshells time to circulate and accumulate. An initial dosage of 7.0 $\mu l\, g^{-1}$ body weight (based on the successful treatment dosage of O'Neal's experiment; see above) failed to produce tumor necrosis, but did halt further tumor growth. In contrast, tumors in the control groups showed a dramatic threefold increase in volume. In a second treatment group, where the dose was raised to 8.5 $\mu l\, g^{-1}$, the results were much more favorable, with 93% of the high-dose-treated tumors being thermally ablated and exhibiting total resorption at 21 days, while the control groups experienced the same threefold volume increase as before (Figure 1.22). While the maximum surface temperatures reached

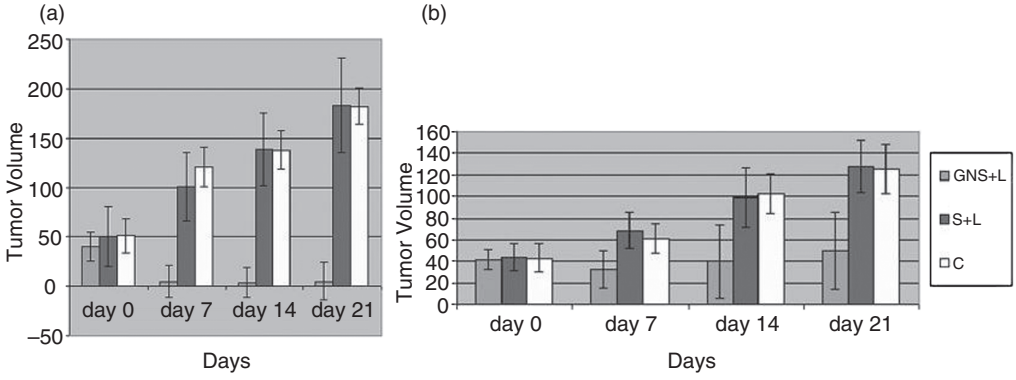

Figure 1.22 (a) High-dose and (b) low-dose treatment groups of gold nanoshells plus laser (GNS+L), saline plus laser (S+L) and negative control (C). A 20% increases in dose leads to a significant different in outcome [85].

65 °C in the nanoshell-rich tumor region, those of the irradiated normal skin areas did not exceed 45 °C. It has been shown that temperatures in excess of 55 °C are required to achieve hyperthermia of prostate cancer cells [103].

The study authors could only speculate as to why one tumor among the 15 treated with the higher dose failed to necrotize, compared to a 100% cure rate in the study of O'Neal. The suggestion was made that an insufficient number of nanoshells had reached the tumor site and, indeed, in a previous *in vitro* study Stern and colleagues had shown that a ratio of 5000 nanoshells per cell was needed to induce thermal necrosis at a fixed intensity [98]. Nonetheless, the results of this study underscore the need for future research to determine optimal dosing schemes.

Elliot *et al*. have modeled nanoshell-mediated photothermal therapy using the diffusion approximation to predict spatiotemporal temperature fluctuations in tissue undergoing therapy [104]. The model was validated using results from tissue phantom experiments, and predicted measured temperature values with reasonable accuracy. However, it did not account for those factors present under *in vivo* conditions, such as blood perfusion. However, in looking to the future, a quantitative *in vivo* model of nanoshell-mediated photothermal therapy will surely be very helpful in tailoring individual treatment regimens to human patients.

1.5.6 Drug Delivery

Nanoshells have long shown promise for increasing drug delivery to tumors. Shetty *et al*. have demonstrated enhanced tumor perfusion in mice with xenografted prostate tumors, the perfusion being increased by nanoshell-mediated heating [105]. Mice were injected with nanoshells at 24 h before laser treatment, and perfusion was monitored using MRI. Whereas, heating with low (0.8 W cm^{-2}) and high (4 W cm^{-2}) laser intensities decreased contrast uptake, heating with an intensity of 2 W cm^{-2} almost doubled the uptake, thus highlighting the potential of nanoshells for improving drug delivery.

Nanoshells have also been demonstrated to modulate drug delivery. For example, Sershen *et al*. incorporated nanoshells with an 832 nm resonance into a thermally responsive polymer, *N*-isopropylacrylamide-*co*-acrylamide (NIPAAm), to create a photomediated drug delivery hydrogel composite [106, 107]. Hydrogels based on NIPAAm exhibit a lower critical solution temperature above which the hydrogel undergoes a reversible volume phase change transition. The nanoshells used in the experiment were engineered to have a core radius of 50 nm and shell thickness of 7 nm, in order to maximize absorption. When the composite is illuminated with a diode laser at 832 nm, the nanoshells convert light into heat, inducing a reversible and repeatable light-driven collapse of the composite hydrogel matrix. After 40 min of irradiation at 1.8 W cm^{-2}, the hydrogel composite had shrunk to 10% of its initial weight (Figure 1.23).

Recently, Bikram *et al*. demonstrated the potential value of nanoshell composites as drug delivery vehicles in specific applications [108]. In this case, hydrogels

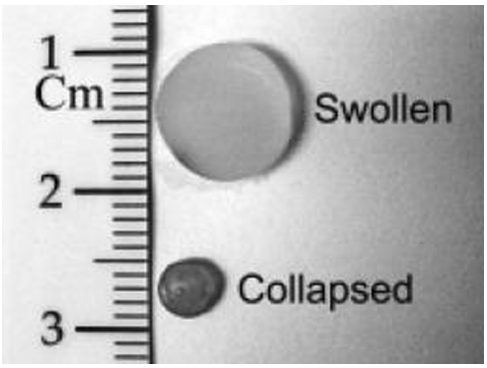

Figure 1.23 Swollen and collapsed nanoshell–polymer hydrogels. The change in volume is induced by heating [107].

containing 10^9 nanoshells ml^{-1} were swollen in solutions containing 10 mg ml^{-1} insulin, lysozyme and methylene blue, which was used as a model drug. When the release of each compound was monitored before and after laser irradiation, the release profiles of the embedded drugs upon irradiation were found to depend on their molecular weights. The release of methylene blue (14.1 mg g^{-1} polymer) and insulin (12.9 mg g^{-1}) occurred spontaneously, but the release of lysozyme occurred only upon laser irradiation. Moreover, the amounts of insulin and methylene blue released were approximately doubled on irradiation. Taken together, these results indicate that nanoshell-composite hydrogels have great potential for future drug delivery applications.

1.5.7
Tissue Welding

Nanoshells may represent a rapid means of treating lacerations in an emergency room setting. As an example, Gobin *et al*. have used nanoshells as an exogenous NIR absorber for welding deep tissue wounds [109]. In this study, a nanoshell-based solder (nanoshells + bovine serum albumin (BSA)) was applied to full-thickness incisions made on rats, after which the incisions were irradiated with NIR laser light for several minutes to initiate tissue welding. Notably, the healing results were similar to the suture–treat control group until day 5, after which healing was shown to be better in the suture group.

1.5.8
Biosensors

Nanoshells have several unique properties that are ideal for biosensing applications. The position of the plasmon resonance peak and absorbance depended heavily on the refractive index (dielectric constant) of the surrounding medium,

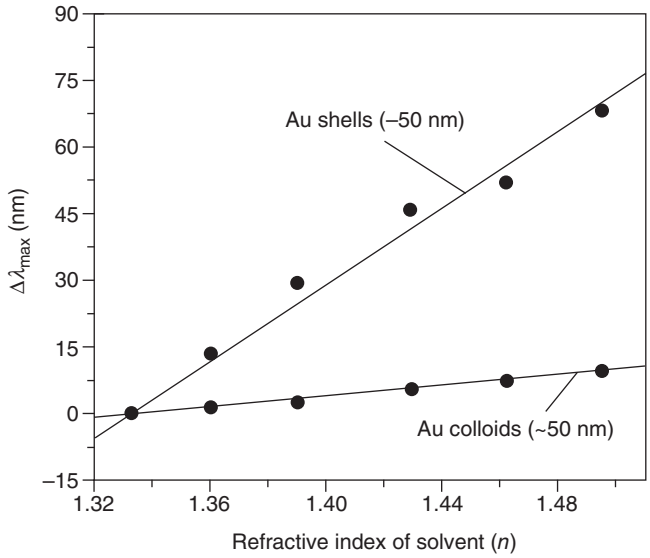

Figure 1.24 Linear relationship between shift in resonance peak and change in the index of refraction (n) of the surrounding environment. Nanoshells show greater sensitivity than nanospheres [70].

which is predicted by Mie theory [13]. As an example, Sun *et al.* have shown that gold nanoshells are more sensitive than nanospheres to changes in the refractive index (n) of the surrounding environment, and that the observed peak shift varies linearly with n [110] (Figure 1.24). In an aqueous medium, a 10% change in n corresponds to a substantial peak shift of approximately 50 nm – a finding which is consistent with the results of Tam *et al.*, who measured sensitivities of up to $\Delta\lambda/\Delta n = 555.4$ [111]. Thus, nanoshells exhibit optical sensitivity to the surrounding environment, a property which may be exploited to detect biomarkers in simple absorbance assays [112, 113].

Nanoshells can also be used to render conventional fluorophores sensitive to the surrounding environment, while protecting them from degradation. Recently, Chen *et al.* observed a fivefold enhancement of the fluorescence efficiency of a tetramethyl rhodamine dye molecule embedded within the silica core of a nanoshell [114]. The peak wavelength of the fluorophore was shifted by over 50 nm when the refractive index of the surrounding medium changed from 1.3 to 1.6.

Nanoshells are also capable of immensely amplifying SERS signals [31, 115] by many orders of magnitude (10^{12}–10^{15}) through strong electromagnetic near-field enhancement [13, 18], thus enabling exquisite detection in the picomolar range [116]. Typically, Raman signal strength scales as the electric field to the fourth power (E^4). The following examples serve to highlight the two primary methods for using nanoshells in biosensing schemes, namely absorbance and SERS measurements.

1.5.8.1 Absorbance-Based Biosensing

Several groups have demonstrated the use of biosensors for quantifying protein concentrations in diluted human whole blood, using bioconjugated nanoshells. Neither of the following applications requires any sample preparation, which represents a major advantage over other immunoassay techniques, such as enzyme-linked immunosorbent assay (ELISA). Wang *et al.* have developed a biosensor based on self-assembled gold nanoshell monolayers to optically transduce interactions between the vitamin biotin and streptavidin (a tetrameric bacterial protein) in a 20% blood solution [113]. The monolayer was grown on an APTES (amine-functionalized) glass slide, immersed in a cystamine solution, and then reacted with biotin–*N*-hydroxysuccinimide in a DMSO solution. After blocking with BSA to prevent nonspecific adsorption, the sensor was exposed to 20% whole blood with different concentrations of streptavidin for 1 h. Absorbance changes at 730 nm were measured with a UV/visible spectrophotometer in transmission mode. In this way, the sensor proved capable of the accurate and reproducible detection of streptavidin at concentrations ranging from 3 to 50 $\mu g\,ml^{-1}$.

Hirsch *et al.* have developed a nanoshell absorbance-based sensor, capable of detecting very low ($ng\,ml^{-1}$) concentrations of multivalent antigens in whole blood within 10–30 min [112]. This detection scheme is based on monitoring changes in the UV/visible spectrum as the analyte binding proceeds. Such binding results in nanoshell aggregation, which leads in turn to a decrease in extinction and a red-shifted broadening of the plasmon resonance peak [96]. In this experiment, PEGylated nanoshells were functionalized with rabbit anti-IgG, and the immunoassay was carried out to detect rabbit IgG successfully in 20% human whole blood, with a detection limit of 4.4 $ng\,ml^{-1}$ and good reproducibility.

Recently, Shuford *et al.* have developed and characterized a new variety of nanoshell, namely 'gold pyramidal shells' which, unlike their spherical brethren, are larger (~300 nm diameter), exhibit orientation-dependent spectra, and possess a unique TE-like plasmon mode in addition to the standard dipole and quadrapole resonances [117]. As the TE-like plasmon mode disappears when the pyramid's apex is altered, the authors speculated that pyramidal shells could be used in a 'sandwich' assay, in which the analyte binds to the tip and base of the pyramid.

1.5.8.2 SERS Biosensing

Qian *et al.* have demonstrated intense SERS signal enhancements using nanoshells for cancer cell detection [65]. PEGylated nanospheres with Raman reporter 3,3′-diethylthiatricarbocyanine iodide (DTTC), a NIR dye, were conjugated with EGFR antibody and incubated with head and neck Tu686 carcinoma cells. The PEGylated nanospheres enhanced the SERS signal enough to permit Raman molecular profiling studies of single cancer cells. For comparison, the nanoshells were found to be three times brighter than NIR-emitting quantum dots on a per volume basis, and more than 200 times brighter on a per particle basis, thus demonstrating the utility of nanoshells in sensitive detection schemes.

Beier *et al.* have investigated the use of gold nanoshell-based SERS as a novel platform for diagnosing Alzheimer's disease in its earliest stages, by detecting structure-specific forms of β-amyloid peptide, a biomolecule thought to be present

in the cerebrospinal fluid in miniscule, but pathologically distinguishable, concentrations [116]. β-Amyloid, which is a signature biomarker of the disease, aggregates to form senile plaques in the brains of Alzheimer's patients. At present, there is no method available for the definitive diagnosis of Alzheimer's disease pre-mortem, as any probable diagnosis is based on MRI imaging of the brain and cognitive function tests [118]. In this experiment, nanoshells were deposited uniformly onto a glass slide to form a monolayer, and then functionalized with cystamine bound to sialic acid, which has a high affinity for β-amyloid. The nanoshell slide was then immersed in solutions containing known amounts of β-amyloid for 30–45 min to permit binding. After rinsing, the slides were exposed to Congo Red, a SERS-active NIR dye which binds specifically to β-amyloid. After another round of rinsing, SERS measurements were performed, producing signal intensities sufficient for the detection of β-amyloid at concentrations as low as 1 p*M*. However, the signal contrast was not high enough to permit a definitive determination of concentration, which would certainly be valuable from a diagnostic standpoint.

In recent years, nanoshells and other gold nanoparticles have shown great promise as biosensors for quantifying very low concentrations of biomarkers, although many more investigations are required in order to refine this nascent technology for specific clinical applications.

1.6 Concluding Remarks

Because of their unique features and vast potential for a variety of biomedical applications, gold nanoshells and other gold nanoparticles represent a major achievement in nanotechnology. The synergy of ideal chemical, physical and optical properties in a single particle is a resounding affirmation of the promise of nanotechnology in general.

Gold nanoshells have opened new frontiers in medicine. Because they are biocompatible, optically tunable, strongly photoluminescent and bind to antibodies, nanoshells are highly suitable for *in vivo* imaging studies. Likewise, because they accumulate within tumors due to passive and active mechanisms, they hold great promise for revolutionizing cancer detection. Their success in multiple animal studies has confirmed a great potential as agents for photothermal cancer therapy, with the added benefit of serving as contrast agents for cancer detection. Clinical trials, which are currently under way, will most likely establish their efficacy for the treatment of human forms of cancer.

However, there are several pressing research problems, which are yet to be investigated. For example, what is the largest size tumor that nanoshells can effectively treat? And, can patient-specific antibodies be targeted to enhance their efficacy? It is hoped that, in the near future, these questions will be addressed and the novel properties of nanoshells will continue to be exploited in a growing number of applications. Clearly, it will be very exciting to see many existing applications make the successful transition from the laboratory bench to the clinic.

References

1 Park, J., Estrada, A., Sharp, K., Sang, K., Schwartz, J.A., Smith, D.K., Coleman, C., Payne, J.D., Korgel, B.A., Dunn, A.K. and Tunnell, J.W. (2008) Two-photon-induced photoluminescence imaging of tumors using near-infrared excited gold nanoshells. *Optics Express*, **16**, 1590–9.

2 Nanospectra Biosciences Inc. (2008) www.nanospectra.com (last accessed 26 June 2008)

3 Wu, C., Liang, X. and Jiang, H. (2005) Metal nanoshells as a contrast agent in near-infrared diffuse optical tomography. *Optics Communications*, **253**, 214–21.

4 Hirsch, L.R., Stafford, R.J., Bankson, J.A., Sershen, S.R., Rivera, B., Price, R.E., Hazle, J.D., Halas, N.J. and West, J.L. (2003) Nanoshell-mediated near-infrared thermal therapy of Tumors under magnetic resonance guidance. *Proceedings of the National Academy of Sciences of the United States of America*, **100**, 13549–54.

5 Leatherdale, C.A., Woo, W.K., Mikulec, F.V. and Bawendi, M.G. (2002) On the absorption cross section of CdSe nanocrystal quantum dots. *The Journal of Physical Chemistry B*, **106**, 7619–22.

6 Jain, P.K., Lee, K.S., El-Sayed, I.H. and El-Sayed, M.A. (2006) Calculated absorption and scattering properties of gold nanoparticles of different size, shape, and composition: applications in biological imaging and biomedicine. *The Journal of Physical Chemistry B*, **110**, 7238–48.

7 Wang, H., Huff, T.B., Zweifel, D.A., He, W., Low, P.S., Wei, A. and Cheng, J.X. (2005) In vitro and in vivo two-photon luminescence imaging of single gold nanorods. *Proceedings of the National Academy of Sciences of the United States of America*, **102**, 15752–6.

8 Yguerabide, J. and Yguerabide, E.E. (2001) Resonance light scattering particles as ultrasensitive labels for detection of analytes in a wide range of applications. *Journal of Cellular Biochemistry*, **84**, 71–81.

9 Eggeling, C., Widengren, J., Rigler, R. and Seidel, C.A.M. (1998) Photobleaching of fluorescent dyes under conditions used for single-molecule detection: evidence of two-step photolysis. *Analytical Chemistry*, **70**, 2651–9.

10 Widengren, J. and Rigler, R. (1996) Mechanisms of photobleaching investigated by fluorescence correlation spectroscopy. *Bioimaging*, **4**, 149–57.

11 Chan, W.C.W. and Nie, S. (1998) Quantum dot bioconjugates for ultrasensitive nonisotopic detection. *Science*, **281**, 2016.

12 Hohng, S. and Ha, T. (2004) Near-complete suppression of quantum dot blinking in ambient conditions. *Journal of the American Chemical Society*, **126**, 1324–5.

13 Averitt, R.D., Westcott, S.L. and Halas, N.J. (1999) Linear optical properties of gold nanoshells. *Journal of the Optical Society of America B*, **16**, 1824–32.

14 Stolik, S., Delgado, J.A., Pérez, A. and Anasagasti, L. (2000) Measurement of the penetration depths of red and near infrared light in human 'ex vivo' tissues. *Journal of Photochemistry & Photobiology B: Biology*, **57**, 90–3.

15 Ntziachristos, V., Ripoll, J., Wang, L.V. and Weissleder, R. (2005) Looking and listening to light: the evolution of whole-body photonic imaging. *Nature Biotechnology*, **23**, 313–20.

16 Chien, W.Y. and Szkopek, T. (2008) Multiple-multipole simulation of optical nearfields in discrete metal nanosphere assemblies. *Optics Express*, **16**, 1820–35.

17 Oldenburg, S.J., Hale, G.D., Jackson, J.B. and Halas, N.J. (1999) Light scattering from dipole and quadrupole nanoshell antennas. *Applied Physics Letters*, **75**, 1063.

18 Jackson, J.B., Westcott, S.L., Hirsch, L.R., West, J.L. and Halas, N.J. (2003) Controlling the surface enhanced Raman effect via the nanoshell geometry. *Applied Physics Letters*, **82**, 257.

19 Novotny, L. and Hecht, B. (2006) *Principles of Nano-Optics*, Cambridge University Press, Cambridge.

20 Mie, G. (1908) Beiträge zur Optik trüber Medien, speziell kolloidaler Metallösungen. *Annalen der Physik*, **330**, 377–445.

21 Prodan, E., Radloff, C., Halas, N.J. and Nordlander, P. (2003) *A Hybridization Model for the Plasmon Response of Complex Nanostructures*, American Association for the Advancement of Science, pp. 419–22.

22 Johnson, P.B. and Christy, R.W. (1972) Optical constants of the noble metals. *Physical Review B*, **6**, 4370–9.

23 Vial, A., Grimault, A.S., Macías, D., Barchiesi, D. and de la Chapelle, M.L. (2005) Improved analytical fit of gold dispersion: application to the modeling of extinction spectra with a finite-difference time-domain method. *Physical Review B*, **71**, 85416.

24 Jensen, T.R., Malinsky, M.D., Haynes, C.L. and Van Duyne, R.P. (2000) Nanosphere lithography: tunable localized surface plasmon resonance spectra of silver nanoparticles. *The Journal of Physical Chemistry B*, **104**, 10549–56.

25 Ishimaru, A. (1978) *Wave Propagation and Scattering in Random Media*, Academic Press, New York.

26 Westcott, S.L., Jackson, J.B., Radloff, C. and Halas, N.J. (2002) Relative contributions to the plasmon line shape of metal nanoshells. *Physical Review B*, **66**, 155431.

27 Nehl, C.L., Grady, N.K., Goodrich, G.P., Tam, F., Halas, N.J. and Hafner, J.H. (2004) Scattering spectra of single gold nanoshells. *Nano Letters*, **4**, 2355–9.

28 Haus, J.W., Zhou, H.S., Takami, S., Hirasawa, M., Honma, I. and Komiyama, H. (1993) Enhanced optical properties of metal-coated nanoparticles. *Journal of Applied Physics*, **73**, 1043.

29 van de Hulst, H.C. (1957) *Light Scattering by Small Particles. Light Scattering by Small Particles*, John Wiley & Sons, Inc., New York.

30 Aden, A.L. and Kerker, M. (2004) Scattering of electromagnetic waves from two concentric spheres. *Journal of Applied Physics*, **22**, 1242.

31 Campion, A. and Kambhampati, P. (1998) Surface-enhanced Raman scattering. *Chemical Society Reviews*, **27**, 241–50.

32 Beversluis, M.R., Bouhelier, A. and Novotny, L. (2003) Continuum generation from single gold nanostructures through near-field mediated intraband transitions. *Physical Review B*, **68**, 115433.

33 Boyd, G.T., Yu, Z.H. and Shen, Y.R. (1986) Photoinduced luminescence from the noble metals and its enhancement on roughened surfaces. *Physical Review B*, **33**, 7923–36.

34 Mooradian, A. (1969) Photoluminescence of metals. *Physical Review Letters*, **22**, 185–7.

35 Mohamed, M.B., Volkov, V., Link, S. and El-Sayed, M.A. (2000) The lightning rod effect in gold nanorods: fluorescence enhancement of over a million compared to the gold metal. *Chemical Physics Letters*, **317**, 517–23.

36 Clarke, M.., Kang, H., Yim, P., Kishore, R., Helmerson, K. and Hwang, J. (2008) Thermal properties of gold nanoshells in lipid vesicles studied by single particle tracking measurements. *Proceedings of SPIE*, **6849**, 68490H/1–68490H/9.

37 Aguirre, C.M., Moran, C.E., Young, J.F. and Halas, N.J. (2004) Laser-induced reshaping of metallodielectric nanoshells under femtosecond and nanosecond plasmon resonant illumination. *Journal of Physical Chemistry B*, **108**, 7040–5.

38 Kamat, P.V., Flumiani, M. and Hartland, G.V. (1998) Picosecond dynamics of silver nanoclusters. Photoejection of electrons and fragmentation. *The Journal of Physical Chemistry B*, **102**, 3123–8.

39 Lin, A., Hirsch, L., Lee, M.H., Barton, J., Halas, N., West, J. and Drezek, R. (2004) Nanoshell-enabled photonics-based imaging and therapy of cancer. *Technology in Cancer Research & Treatment*, **3**,

40 Oldenburg, S.J., Averitt, R.D., Westcott, S.L. and Halas, N.J. (1998) Nanoengineering of optical resonances. *Chemical Physics Letters*, **288**, 243–7.

41 Neeves, A.E. and Birnboim, M.H. (1989) Composite structures for the enhancement of nonlinear-optical susceptibility. *Journal of the Optical Society of America B: Optical Physics*, **6**, 787–96.

42 Averitt, R.D., Oldenburg, S.J., Halas, N.J., Sershen, S.R. and West, J.L. (2002) Temperature-sensitive polymer/nanoshell composites for photothermally. US Patent 6,428,811.

43 Oldenburg, S.J., Averitt, R.D. and Halas, N.J. (2004) Metal nanoshells. US Patent 6344272.

44 West, J.L., Halas, N.J., Oldenburg, S.J. and Averitt, R.D. (2004) Metal nanoshells for biosensing applications. US Patent 6699724.

45 West, J.L., Drezek, R., Sershen, S. and Halas, N.J. (2004) Optically-absorbing nanoparticles for enhanced tissue repair. US Patent 6685730.

46 Pham, T., Jackson, J.B., Halas, N.J. and Lee, T.R. (1998) Preparation and characterization of gold nanoshells coated with self-assembled monolayers. *Physics Letters*, **288**, 243.

47 Stober, W., Fink, A. and Bohn, E. (1968) Controlled growth of monodisperse silica spheres in the micron size range. *Journal of Colloid and Interface Science*, **26**, 62–9.

48 Duff, D.G., Baiker, A. and Edwards, P.P. (1993) A new hydrosol of gold clusters. 1. Formation and particle size variation. *Langmuir*, **9**, 2301–9.

49 Leff, D.V., Brandt, L. and Heath, J.R. (1996) Synthesis and characterization of hydrophobic, organically-soluble gold nanocrystals functionalized with primary amines. *Langmuir*, **12**, 4723–30.

50 Roosen, A.R. and Carter, W.C. (1998) Simulations of microstructural evolution: anisotropic growth and coarsening. *Physica A*, **261**, 232–47.

51 Phonthammachai, N., Kah, J., Jun, G., Sheppard, C., Olivo, M., Mhaisalkar, S., White, T. (2008) Synthesis of contiguous silica-gold core-shell structures: critical parameters and processes. *Langmuir*, **24** (9), 5109–12.

52 Wang, H., Goodrich, G., Tam, F., Oubre, C., Nordlander, P. and Halas, N.J. (2005) Controlled texturing modifies the surface topography and plasmonic properties of Au nanoshells. *Journal of Physical Chemistry B*, **109**, 11083–7.

53 Tang, L., Liu, L. and Elwing, H.B. (1998) Complement activation and inflammation triggered by model biomaterial surfaces. *Journal of Biomedical Materials Research*, **41**, 333–40.

54 Loo, C., Hirsch, L., Lee, M.H., Chang, E., West, J., Halas, N. and Drezek, R. (2005) Gold nanoshell bioconjugates for molecular imaging in living cells. *Optics Letters*, **30**, 1012–14.

55 Sokolov, K., Follen, M., Aaron, J., Pavlova, I., Malpica, A., Lotan, R. and Richards-Kortum, R. (2003) Real-time vital optical imaging of precancer using anti-epidermal growth factor receptor antibodies conjugated to gold nanoparticles 1. *Cancer Research*, **63**, 1999–2004.

56 Burns, R. (2005) *Immunochemical Protocols; Methods in Microbiology*, Humana Press.

57 Kumar, S., Aaron, J. and Sokolov, K. (2008) Directional conjugation of antibodies to nanoparticles for synthesis of multiplexed optical contrast agents with both delivery and targeting moieties. *Nature Protocols*, **3**, 314–20.

58 Jain, R.K. (1999) Transport of molecules, particles, and cells in solid tumors. *Annual Review of Biomedical Engineering*, **1**, 241–63.

59 James, W.D., Hirsch, L.R., West, J.L., O'Neal, P.D. and Payne, J.D. (2007) Application of INAA to the build-up and clearance of gold nanoshells in clinical studies in mice. *Journal of Radioanalytical and Nuclear Chemistry*, **271**, 455–9.

60 Zaman, R.T., Diagaradjane, P., Wang, J.C., Schwartz, J., Rajaram, N., Gill-Sharp, K.L., Cho, S.H., Rylander, H.G., III, Payne, J.D., Krishnan, S. and Tunnell, J.W. (2007) In vivo detection of gold nanoshells in tumors using diffuse optical spectroscopy. *IEEE Journal*, **13**, 1715–20.

61 Xie, H., Gill-Sharp, K.L. and O'Neal, D.P. (2007) Quantitative estimation of gold nanoshell concentrations in whole blood using dynamic light scattering. *Nanomedicine: Nanotechnology, Biology, and Medicine*, **3**, 89–94.

62 Dvorak, H.F., Nagy, J.A., Dvorak, J.T. and Dvorak, A.M. (1988) Identification and characterization of the blood vessels of solid tumors that are leaky to circulating macromolecules. *American Journal of Pathology*, **133**, 95–109.

63 Dedrick, R.L. (1973) Animal scale-up. *Journal of Pharmacokinetics and Pharmacodynamics*, **1**, 435–61.

64 Iyer, A.K., Khaled, G., Fang, J. and Maeda, H. (2006) Exploiting the enhanced permeability and retention effect for tumor targeting. *Drug Discovery Today*, **11**, 812–18.

65 Qian, X., Peng, X.H., Ansari, D.O., Yin-Goen, Q., Chen, G.Z., Shin, D.M., Yang, L., Young, A.N., Wang, M.D. and Nie, S. (2008) In vivo tumor targeting and spectroscopic detection with surface-enhanced Raman nanoparticle tags. *Nature Biotechnology*, **26**, 83–90.

66 Hainfeld, J.F., Slatkin, D.N., Focella, T.M. and Smilowitz, H.M. (2006) Gold nanoparticles: a new X-ray contrast agent. *British Journal of Radiology*, **79**, 248.

67 Hobbs, S.K., Monsky, W.L., Yuan, F., Roberts, W.G., Griffith, L., Torchilin, V.P. and Jain, R.K. (1998) Regulation of transport pathways in tumor vessels: role of tumor type and microenvironment. *Proceedings of the National Academy of Sciences*, **95**, 4607.

68 Niidome, T., Yamagata, M., Okamoto, Y., Akiyama, Y., Takahashi, H., Kawano, T., Katayama, Y. and Niidome, Y. (2006) PEG-modified gold nanorods with a stealth character for in vivo applications. *Journal of Controlled Release*, **114**, 343–7.

69 De Jong, W.H., Hagens, W.I., Krystek, P., Burger, M.C., Sips, A. and Geertsma, R.E. (2008) Particle size-dependent organ distribution of gold nanoparticles after intravenous administration. *Biomaterials*, **29** (12), 1912–19.

70 Fu, K., Sun, J., Bickford, L.R., Lin, A.W.H., Halas, N.J., Yu, T.K. and Drezek, R.A. (2008) Measurement of immunotargeted plasmonic nanoparticles' cellular binding: a key factor in optimizing diagnostic efficacy. *Nanotechnology*, **19**, 45103–9.

71 Choyke, P.L. and Kobayashi, H. (2006) Functional magnetic resonance imaging of the kidney using macromolecular contrast agents. *Abdominal Imaging*, **31**, 224–31.

72 Lewinski, N., Colvin, V. and Drezek, R. (2008) Cytotoxicity of nanoparticles. *Small*, **4**, 26–49.

73 Cai, W., Hsu, A.R., Li, Z.B. and Chen, X. (2007) Are quantum dots ready for in vivo imaging in human subjects? *Nanoscale Research Letters*, **2**, 265–81.

74 McDonald, D.M. and Baluk, P. (2002) Significance of blood vessel leakiness in cancer 1. *Cancer Research*, **62**, 5381–5.

75 Hashizume, H., Baluk, P., Morikawa, S., McLean, J.W., Thurston, G., Roberge, S., Jain, R.K. and McDonald, D.M. (2000) Openings between defective endothelial cells explain tumor vessel leakiness. *American Journal of Pathology*, **156**, 1363–80.

76 Yuan, F. (1995) Vascular permeability in a human tumor xenograft: molecular size dependence and cutoff size. *Cancer Research*, **55**, 3752–6.

77 Jain, R.K. (1987) Transport of molecules across tumor vasculature. *Cancer and Metastasis Reviews*, **6**, 559–93.

78 Monsky, W.L., Fukumura, D., Gohongi, T., Ancukiewcz, M., Weich, H.A., Torchilin, V.P., Yuan, F. and Jain, R.K. (1999) Augmentation of transvascular transport of macromolecules and nanoparticles in tumors using vascular endothelial growth factor 1. *Cancer Research*, **59**, 4129–35.

79 Li, M.L., Schwartz, J.A., Wang, J., Stoica, G. and Wang, L.V. (2007) In-vivo imaging of nanoshell extravasation from solid tumor vasculature by photoacoustic microscopy. *Proceedings of SPIE*, **6437**, 64370B.

80 Padera, T.P., Stoll, B.R., Tooredman, J.B., Capen, D., di Tomaso, E. and Jain, R.K. (2004) Pathology: cancer cells compress intratumour vessels. *Nature*, **427**, 695.

81 Merchant, B. (1998) Gold, the noble metal and the paradoxes of its toxicology. *Biologicals*, **26**, 49–59.

82 Choi, J., Burns, A.A., Williams, R.M., Zhou, Z., Flesken-Nikitin, A., Zipfel, W.R., Wiesner, U. and Nikitin, A.Y. (2007) Core-shell silica nanoparticles as fluorescent labels for nanomedicine. *Journal of Biomedical Optics*, **12**, 064007.

83 Shukla, R., Bansal, V., Chaudhary, M., Basu, A., Bhonde, R.R. and Sastry, M. (2005) Biocompatibility of gold

nanoparticles and their endocytotic fate inside the cellular compartment: a microscopic overview. *Langmuir*, **21**, 10644–54.

84 O'Neal, D.P., Hirsch, L.R., Halas, N.J., Payne, J.D. and West, J.L. (2004) Photo-thermal tumor ablation in mice using near infrared-absorbing nanoparticles. *Cancer Letters*, **209**, 171–6.

85 Stern, J.M., Stanfield, J., Kabbani, W., Hsieh, J.T. and Cadeddu, J.A. (2008) Selective prostate cancer thermal ablation with laser activated gold nanoshells. *The Journal of Urology*, **179**, 748–53.

86 Balduzzi, M., Diociaiuti, M., De Berardis, B., Paradisi, S. and Paoletti, L. (2004) In vitro effects on macrophages induced by noncytotoxic doses of silica particles possibly relevant to ambient exposure. *Environmental Research*, **96**, 62–71.

87 Shiohara, A., Hoshino, A., Hanaki, K., Suzuki, K. and Yamamoto, K. (2004) On the cyto-toxicity caused by quantum dots. *Microbiology and Immunology*, **48**, 669–75.

88 Etzioni, R., Urban, N., Ramsey, S., McIntosh, M., Schwartz, S., Reid, B., Radich, J., Anderson, G. and Hartwell, L. (2003) The case for early detection. *Nature Reviews Cancer*, **3**, 243–52.

89 Aaron, J., Nitin, N., Travis, K., Kumar, S., Collier, T., Park, S.Y., José-Yacamán, M., Coghlan, L., Follen, M. and Richards-Kortum, R. (2007) Plasmon resonance coupling of metal nanoparticles for molecular imaging of carcinogenesis in vivo. *Journal of Biomedical Optics*, **12**, 034007.

90 Loo, C., Lowery, A., Halas, N., West, J. and Drezek, R. (2005) Immunotargeted nanoshells for integrated cancer imaging and therapy. *Nano Letters*, **5**, 709–11.

91 Durr, N.J., Larson, T., Smith, D.K., Korgel, B.A., Sokolov, K. and Ben-Yakar, A. (2007) Two-photon luminescence imaging of cancer cells using molecularly targeted gold nanorods. *Nano Letters*, **7**, 941–5.

92 El-Sayed, I.H., Huang, X. and El-Sayed, M.A. (2006) Selective laser photo-thermal therapy of epithelial carcinoma using anti-EGFR antibody conjugated gold nanoparticles. *Cancer Letters*, **239**, 129–35.

93 El-Sayed, I.H., Huang, X. and El-Sayed, M.A. (2005) Surface plasmon resonance scattering and absorption of anti-EGFR antibody conjugated gold nanoparticles in cancer diagnostics: applications in oral cancer. *Nano Letters*, **5**, 829–34.

94 Mallidi, S., Larson, T., Aaron, J., Sokolov, K. and Emelianov, S. (2007) Molecular specific optoacoustic imaging with plasmonic nanoparticles. *Optics Express*, **15**, 6583–8.

95 Fournelle, M., Maass, K., Fonfara, H., Welsch, H.J., Hewener, H., Gunther, C. and Lemor, R.M. (2007) P6A-5 real-time optoacoustic imaging using near infrared absorbing gold nanoshells for contrast enhancement, Ultrasonics Symposium, IEEE, pp. 2417–20.

96 Rechberger, W., Hohenau, A., Leitner, A., Krenn, J.R., Lamprecht, B. and Aussenegg, F.R. (2003) Optical properties of two interacting gold nanoparticles. *Optics Communications*, **220**, 137–41.

97 Gobin, A.M., Lee, M.H., Halas, N.J., James, W.D., Drezek, R.A. and West, J.L. (2007) Near-infrared resonant nanoshells for combined optical imaging and photothermal cancer therapy. *Nano Letters*, **7**, 1929–34.

98 Stern, J.M. and Cadeddu, J.A. (2008) Emerging use of nanoparticles for the therapeutic ablation of urologic malignancies. *Urologic Oncology: Seminars and Original Investigations*, **26**, 93–6.

99 Everts, M., Saini, V., Leddon, J.L., Kok, R.J., Stoff-Khalili, M., Preuss, M.A., Millican, C.L., Perkins, G., Brown, J.M. and Bagaria, H. (2006) Covalently linked Au nanoparticles to a viral vector: potential for combined photothermal and gene cancer therapy. *Nano Letters*, **6**, 587–91.

100 Chance, B. (1991) Optical method. *Annual Review of Biophysics and Biophysical Chemistry*, **20**, 1–30.

101 Welch, A.J. and van Gemert, M.J.C. (1995) *Optical-thermal Response of Laser-irradiated Tissue*, Plenum Publishing Corp.

102 Diagaradjane, P, Shetty, A., Wang, J., Elliot, A., Schwartz, J., Shentu, S., Park,

C., Deorukhkar, A., Stafford, J., Cho, S., Tunnell, J.W., Hazle, J. and Krishnan, S. (2008) Gold nanoshell mediated hyperthermia enhances the efficacy of radiation therapy. *Proceedings of the SPIE*, **6895**, 68650N.

103 Patriarca, C., Bergamaschi, F., Gazzano, G., Corrada, P., Ordesi, G., Zanitzer, L., Di Pasquale, M., Giunta, P. and Campo, B. (2006) Histopathological findings after radiofrequency (RITA) treatment for prostate cancer. *Prostate Cancer and Prostatic Diseases*, **9**, 266–9.

104 Elliott, A.M., Stafford, R.J., Schwartz, J., Wang, J., Shetty, A.M., Bourgoyne, C., O'Neal, P. and Hazle, J.D. (2007) Laser-induced thermal response and characterization of nanoparticles for cancer treatment using magnetic resonance thermal imaging. *Medical Physics*, **34**, 3102.

105 Shetty, A., Elliott, A.M., Schwartz, J.A., Wang, J., Esparza-Coss, E., Klumpp, S., Taylor, B., Hazle, J.D. and Stafford, R.J. (2008) Use of gold nanoshells to mediate heating induced perfusion changes in prostate tumors. *Proceedings of SPIE*, **6842**, 68420S.

106 Sershen, S.R., Westcott, S.L., Halas, N.J. and West, J.L. (2002) Independent optically addressable nanoparticle-polymer optomechanical composites. *Applied Physics Letters*, **80**, 4609.

107 Sershen, S.R., Westcott, S.L., West, J.L. and Halas, N.J. (2001) An opto-mechanical nanoshell-polymer composite. *Applied Physics B: Lasers and Optics*, **73**, 379–81.

108 Bikram, M., Gobin, A.M., Whitmire, R.E. and West, J.L. (2007) Temperature-sensitive hydrogels with SiO_2–Au nanoshells for controlled drug delivery. *Journal of Controlled Release*, **123**, 219–27.

109 Gobin, A.M., O'Neal, D.P., Halas, N.J., Drezek, R. and West, J.L. (2005) near infrared laser tissue welding using nanoshells as an exogenous absorber. *Lasers in Surgery and Medicine*, **37**, 123–9.

110 Sun, Y. and Xia, Y. (2003) Synthesis of Gold Nanoshells and Their Use in Sensing Applications. Unconventional Approaches to Nanostructures with Applications in Electronics, Photonics, Information Storage and Sensing, as held at the 2003 MRS Spring Meeting, pp. 31–6.

111 Tam, F., Moran, C. and Halas, N. (2004) Geometrical parameters controlling sensitivity of nanoshell plasmon resonances to changes in dielectric environment. *The Journal of Physical Chemistry B*, **108**, 17290–4.

112 Hirsch, L.R., Jackson, J.B., Lee, A., Halas, N.J. and West, J.L. (2003) A whole blood immunoassay using gold nanoshells. *Analytical Chemistry*, **75**, 2377–81.

113 Wang, Y., Qian, W., Tan, Y. and Ding, S. (2008) A label-free biosensor based on gold nanoshell monolayers for monitoring biomolecular interactions in diluted whole blood. *Biosensors and Bioelectronics*, **23** (7), 1166–70.

114 Chen, X., He, S. and Choy, W. (2008) Highly efficient and tunable fluorescence of a nanofluorophore in silica/metal dual shells with plasmonic resonance. *Journal of Applied Physics*, **103** (2), 024301/1–024301/5.

115 Oldenburg, S.J., Westcott, S.L., Averitt, R.D. and Halas, N.J. (1999) Surface enhanced Raman scattering in the near infrared using metal nanoshell substrates. *The Journal of Chemical Physics*, **111**, 4729.

116 Cowan, C., Theresa, A., Beier, H.T., Cote, G. and Jackson, J.B. (2007) Application of surface enhanced Raman spectroscopy for detection of beta amyloid mediated by sialic acid, The 2007 Annual Meeting.

117 Shuford, K.L.; Lee, J.; Odom, T.W.; Schatz, G.C. (2008) Optical properties of gold pyramidal shells. *Journal of Physical Chemistry C*, **112** (17), 6662–6.

118 McKhann, G. (1984) Clinical diagnosis of Alzheimer's disease: report of the NINCDS-ADRDA Work Group under the auspices of Department of Health and Human Services Task Force on Alzheimer's Disease. *Neurology*, **34**, 939–44.